https://doi.org/10.1016/j.compstruct.2022.116301

COMPRESSIVE BEHAVIOUR OF ELLIPTICAL FRP TUBE-CONFINED CONCRETE COLUMNS

K.C. Liu[a], C. Jiang[a,b], T. Yu[a,*] and J.G. Teng[a,*]

[a]*Department of Civil and Environmental Engineering, The Hong Kong Polytechnic University, Hong Kong, China.*

[b]*Centre for Infrastructure Engineering, Western Sydney University, Penrith, NSW 2751, Australia*

ABSTRACT

Elliptical FRP tube-confined concrete columns (EFCCCs) are an extension of circular FRP tube-confined concrete columns recently proposed at The Hong Kong Polytechnic University. Like their circular counterparts, EFCCCs are corrosion-resistant and can be used in situations where a column is subjected to substantially different loads in the two orthogonal lateral directions. The elliptical section of EFCCCs leads to more effective confinement of the concrete and an easier filament-winding fabrication process for the FRP tube compared with their rectangular counterparts. Existing studies on FRP-confined concrete in elliptical columns have been few. This paper first presents a systematic experimental study on the axial compressive behaviour of EFCCCs, with a focus on the stress-strain behaviour of the confined concrete. The test variables included the concrete strength, the thickness and fibre orientations of the FRP tube, and the aspect ratio of the cross-section. The test results showed that the confinement effectiveness of FRP tubes decreases with the aspect ratio and the concrete strength but increases with the FRP tube thickness. The orientations of fibres in the FRP tube were found to have a significant effect on its confinement effectiveness and the failure mode of EFCCCs. On the basis of the test results, existing stress-strain models for FRP-confined concrete in elliptical columns are evaluated. Furthermore, a new stress-strain model for the concrete in EFCCCs is proposed, which includes a more rigorous treatment of the confinement stiffness of EFCCCs and can provide more accurate predictions for the whole stress-strain curve than the existing models.

Keywords

Elliptical Column; FRP; Concrete; Confinement; Compression; Stress-strain Model.

* Corresponding authors.

Emails: tao-cee.yu@polyu.edu.hk (T. Yu); cejgteng@polyu.edu.hk (J.G. Teng)

1. Introduction

Reinforced concrete columns usually have a circular, square or rectangular cross-section. Columns of circular or square sections are generally used when the required resistances in the two orthogonal lateral directions are similar; otherwise, columns of rectangular sections are preferred. A circular section is generally chosen over a square section because the former is aesthetically more pleasing due to its curved shape than the latter. However, an elliptical section, which is the curved counterpart of a rectangular section, has rarely been used. The lack of popularity of elliptical sections is not surprising given the difficulties associated with the fabrication and/or erection of elliptical formwork.

In recent years, concrete-filled elliptical steel tubular columns have found increasing practical applications [1-7]. This development has been successful because the fabrication/erection of temporary elliptical column formwork is now no longer needed. Based on this development, a new form of columns, namely, elliptical FRP tube-confined concrete columns (EFCCCs) with longitudinal steel reinforcement, have been recently proposed and studied [8] at The Hong Kong Polytechnic University. EFCCCs are attractive for use in structures exposed to a severe environment where steel corrosion is a major issue (e.g., bridges and coastal structures). The FRP tube in an EFCCC serves as a protective skin for the steel reinforcement inside as well as a confining device for the concrete but is not expected to offer longitudinal reinforcement to the concrete. Therefore, these FRP tubes should have fibres oriented close to the hoop direction for them to possess mechanical resistance mainly in the hoop direction. Such FRP tubes are easier to fabricate (e.g., via a filament-winding process) and transport (due to their light weight) than elliptical steel tubes. Therefore, EFCCCs have many advantages over elliptical concrete-filled steel tubes for severe environments, including their excellent corrosion resistance as well as excellent ductility and seismic resistance, all due to the presence of the elliptical FRP tube.

When concrete is confined by an external tube (e.g., steel or FRP tube), the confinement is much more effective for an elliptical section than for a rectangular section [5,9-10]. To develop a reliable design procedure for EFCCCs, it is essential to understand the behaviour of, and to develop a reliable stress-strain model for, the confined concrete in these columns.

The existing research on the stress-strain behaviour of FRP-confined concrete in elliptical columns has been rather limited. To the best of the authors' knowledge, only a small number of experimental studies [9,11-13] were conducted on this topic, and they were limited to the use of wet lay-up FRP wraps with fibres in the hoop direction only. Yan et al. [10] also tested some elliptical specimens where the specimens were shape-modified from rectangular or square ones by an elliptical-section FRP shell and expansive cement. The FRP shell was pre-tensioned by the expansive cement and consequently generated confinement to the inner concrete before testing. Therefore, their results are beyond the scope of this paper. Three design-oriented stress-strain models [11-12,14] were also developed based on all or part of the existing test results, but these models have generally suffered from the limitation of the small test databases available at the time of developing them. In addition, Cao et al. [14] adopted an empirical approach to develop their model in which an elliptical column is converted into a rectangular column; as a result, their model suffers from its complex expressions, and its wide validity is doubtful. The models proposed in Ref. [11-12] are both based on Teng et al.'s model [15] for FRP-confined concrete in circular columns, in which the approach of calculating the second-stage stiffness using the stress and strain at the ultimate state may lead to inaccuracy for the stress-stain path [16].

The latest version of the Chinese national technical standard for the structural use of FRP composites in construction [17] provides a unified stress-strain model which can be used for FRP-confined concrete in elliptical columns. This model is again based on Teng et al.'s model [15] and thus suffers from the same drawback as the models in Ref. [11-12] as explained above.

Against this background, this paper first presents an experimental study on elliptical FRP tube-confined concrete columns (Sections 2 and 3), in which filament-wound FRP tubes with fibres oriented in various angles were used; longitudinal steel reinforcement was not used in the tested specimens as the focus of the tests was on the stress-strain behaviour of the confined concrete in EFCCCs. The existing stress-strain models are then critically assessed using the test results of the present study (Section 4), based on which a new stress-strain model is proposed (Section 5).

2. Experimental program

2.1. Specimen details

A total of 24 elliptical glass FRP (GFRP) tube-confined concrete column specimens were prepared and tested as detailed in Table 1. All the specimens had the same height of 600 mm. The main test variables included the aspect ratio of the section, the concrete strength, and the thickness and fibre orientations of the GFRP tube. The specimens were cast in five batches, and each batch covered the same four aspect ratios ranging from 1.0 to 2.5; these were achieved by varying the minor axis length of the section from 300 mm to 120 mm while keeping the major axis length at 300 mm for all the specimens. Batches A-C were designed to investigate the effect of concrete strength, with the main differences among the three batches being the target concrete strengths, which are 40 MPa, 60 MPa and 80 MPa for batches A-C, respectively. The GFRP tubes used in batches A-C had the same fibre orientations of ±80° to the longitudinal axis of the specimen. Batches D-E were designed to investigate the effect of fibre orientations of GFRP tubes, which were ±60° and ±45° to the longitudinal axis for the two batches of specimens, respectively; the target concrete strength of these two batches was 60 MPa. The GFRP tubes in all the specimens were fabricated with six layers of unidirectional glass fibres, except those in four of the specimens of batch B, which were fabricated with ten layers of unidirectional glass fibres to investigate the effect of FRP tube thickness.

Each specimen is given a name which consists of the following parts in sequence (see Table 1): (1) the letter "E" representing "elliptical column"; (2) a two-digit number (i.e., 10, 15, 20 and 25) representing the aspect ratio (i.e., 1.0, 1.5, 2.0 and 2.5); (3) a letter (i.e., A, B, C, D, or E) as the batch name; (4) the letter "L" followed by a two-digit number (i.e., L06 or L10) indicating the number of fibre layers; and (5) a final two-digit number (i.e., 80, 60, or 45) representing the orientations of fibres in the GFRP tube. For instance, specimen E20B-L06-45 belongs to batch B, had an aspect ratio of 2.0 and was confined by a GFRP tube with six layers of fibres oriented at ±45° to the longitudinal axis.

2.2. Material properties

2.2.1. Concrete

The concrete mix proportions of each batch are summarized in Table 2, with the coarse aggregate having a nominal maximum size of 20 mm. Three plain concrete cylinders were tested for each batch to determine the average concrete compressive strength (f'_{co}) in accordance with ASTM C39 [18] and the corresponding axial strain ε_{co}, the Young's modulus E_c and the Poisson's ratio v in accordance with ASTM C469 [19]. The concrete properties obtained from these tests are summarized in Table 1. It should be noted that batch A was cast using raw materials different from those for other batches, which might have caused the slightly higher E_c value of batch A (f'_{co} = 41.2 MPa) than those of batches B, D and E (f'_{co} = 53.6 – 55.9 MPa).

2.2.2. FRP

The GFRP tubes were prefabricated via a filament winding process by a manufacturer in Guangzhou. (Figure 1). The lengths of the major axis (2*a*) and the minor axis (2*b*) of the steel moulds used to fabricate the GFRP tubes were measured and are listed in Table 3; these values represent the inner dimensions of the GFRP tubes and the outer dimensions of the concrete core. Table 3 also summarizes the thicknesses of all GFRP tubes, each of which is the average value of the measurements at several locations using a Vernier calliper.

To obtain the elastic modulus in the transverse direction of the tubes (i.e., E_t), the so-called curved coupon tests were conducted following Teng et al. [20]. Similar tests have been successfully employed for the same purpose in previous studies [21-22]. The curved coupons all had a width of 30 mm and an arc length of 250 mm and were cut from GFRP tubes of the same batch at locations close to a vertex of the minor axis (Figure

2a). In the tests, the curved coupons were directly pulled at the two ends using an MTS machine (Figures 2b & 2c). The load was applied with a displacement control rate of 6 mm/min before the coupon was straightened, after which the rate was changed to 0.5 mm/min. One bidirectional strain gauge with a gauge length of 5 mm was installed on each side at the middle section of each curved coupon.

Curved coupon tests were first conducted for the six types of elliptical tubes with fibre orientations of ±80°, which covered three aspect ratios (1.5, 2.0 and 2.5) and two numbers of fibre layers (6 layers and 10 layers). Five curved coupons were tested for each type of FRP tube. The key test results are summarized in Table 4, while the typical stress-strain curves are shown in Figures 3a and 3b. It is evident that the stress-strain behaviour is approximately linear as the fibres were close to the transverse direction (Figures 3a and 3b). It should be noted that there is a considerable variation in the thickness of FRP tubes with the same number of fibre layers (Tables 3 and 4), due probably to the difficulty in controlling the volume of resin in the manufacturing of elliptical FRP tubes. This variation led to considerable differences in the elastic moduli of the three groups of specimens with six layers of fibres, which were calculated based on the measured thicknesses (Table 4). Nevertheless, the product of the elastic modulus and the thickness appears to be very similar for the three groups, suggesting that the transverse stiffness of the tubes depends mainly on the volume of fibres and is barely affected by their aspect ratio. Therefore, the transverse stiffness of circular FRP tubes is taken to be equal to that of their elliptical counterparts with the same number of fibre layers.

With the above observation, for the tubes with fibre orientations of ±45° and ±60°, curved coupon tests were only conducted for one aspect ratio (i.e., 1.5). The stress-strain curves of the two types of specimens are shown in Figures 3c and 3d, respectively. It is evident that the curves are significantly nonlinear (Figures 3c and 3d). The elastic moduli, which were calculated using the two points on a stress-strain curve corresponding to the axial strains of 0.001 and 0.003, respectively, are also listed in Table 4 for these specimens. As expected, the elastic modulus in the transverse direction decreases with the fibre orientation angle.

It is worth mentioning that the coupon width might affect the peak hoop stress and the ultimate hoop strain of FRP coupons with a fibre orientation of ±45° and ±60° as how was observed in the split-disk tests [23] of FRP rings with the same fibre orientations in Zhang et al. [24]. In their test, the value of peak hoop stress and ultimate hoop strain was found to increase with the ring width, and that phenomenon was more evident for the FRP rings with a smaller angle of fibre orientation. It was mainly because for FRP rings with a smaller angle of fibre orientation, a larger ring width was needed to not affect the fibre continuity along the hoop direction. Overall, further investigation is needed for determining systematic guidance on the choice of coupon width for FRP tubes with different fibre orientations.

To obtain the mechanical properties in the axial direction, axial compression tests were conducted on 6-layer GFRP rings for the three fibre orientations (±80°, ±60°, ±45°) following the standard GB/T 5350 [25] (Figure 4). The tests were only conducted for the circular GFRP tubes (aspect ratio = 1.0), as the aspect ratio was expected to have little effect on the axial mechanical properties. Three GFRP rings were tested for each type of GFRP tubes. Each FRP ring had a height of 60 mm and was strengthened with carbon FRP (CFRP) strips on both the inner and outer surfaces at its two ends to avoid unexpected local failure. Four axial strain gauges and four hoop strain gauges, which all had a gauge length of 5 mm, were evenly installed around the perimeter at the mid-height of each FRP ring. All specimens were tested using an MTS machine with a displacement control rate of 0.036 mm/min. The dimensions of each specimen were measured at several locations and the average values are given in Table 5.

Figure 5 shows the axial stress-strain curves of FRP rings obtained from these tests, where the axial strains were averaged from the strain gauge readings. It is evident that the initial slope of the curve decreases with the fibre orientation angle (Figure 5). For the FRP rings with fibre orientations of ±80° and ±60°, the curves are almost linear when the axial strain is small but become nonlinear with a decreasing slope afterwards. For the FRP rings with fibre orientations of ±45°, the curve appears to be almost vertical during the late stage of loading. This is because of the significant outward bending of these specimens (Figures 4b and 4c), which led to reductions in the compressive strains on the outer surface of the tube where the strain gauges were attached. Therefore, the final part of the curves does not reflect the true axial compressive properties of the rings. Considering the above observation, the axial strain range from 0.001 to 0.002 was used to calculate the axial elastic modulus and Poisson's ratio for the ±80° and ±60° tubes, while for the ±45° tubes, the axial strain range from 0.0005 to 0.001 was used. The so-obtained results are summarized in Table 5.

2.3. Test setup and instrumentation

For each EFCCC specimen, eight (for circular specimens with an aspect ratio of 1.0) or 12 (for elliptical specimens) transverse strain gauges were installed around the circumference (Figure 6). In addition, four axial strain gauges were installed at 90° apart from each other for each specimen (Figure 6). The strain gauges all had a gauge length of 20 mm and were all located at the mid-height of the specimen. Furthermore, two linear variable differential transformers (LVDTs) were used to obtain the total axial shortening, and another four LVDTs were used to measure the axial deformation of the 240 mm mid-height region of each specimen (Figure 6). Before the test, each of the two ends of the GFRP tube was strengthened with a three-layer, 35 mm wide CFRP strip to avoid local failure in the end region.

The test setup is illustrated in Figure 7. All the specimens were tested using a compression testing machine with a nominal capacity of 8000 kN. The specimens were monotonically loaded with a displacement control rate of 0.36 mm/min.

3. Test results and discussions

3.1. Failure modes

All the specimens were tested to failure except specimen E10B-L10-80, whose test was terminated for safety concerns when the applied load reached 7500 kN, which is close to the capacity of the test machine. As expected, failure was caused by the rupture of the GFRP tube at or close to the mid-height of the specimen in all cases. Figure 8 shows typical specimens after testing. In the specimens with a relatively small aspect ratio and a relatively low concrete strength (e.g., specimen E10B-L06-80 and E15B-L06-80), FRP rupture generally occurred over the whole circumference (Figure 8a). However, as the aspect ratio and/or concrete strength increased, failure tended to localize in a small region close to one of the major axis vertices of the tube (e.g., Figures 8a & 8d.). In addition, after removing the ruptured FRP tubes, it can also be seen that as the aspect ratio increased, the concrete crack tended to exhibit a shear crack pattern (Figure 8f).

For the specimens with ±80° or ±60° fibres, rupture of the FRP tube occurred suddenly with a significant load drop. By contrast, the GFRP rupture of the specimens with ±45° fibres was a more gradual process associated with considerably larger deformation (e.g., Figure 8e), compared with their ±80° and ±60° counterparts. Because of the substantial axial stiffness of the GFRP tubes with ±45° fibres, their failure was sometimes accompanied with local buckling of the FRP tube (Figure 8c), especially for the specimens with a relatively large aspect ratio (e.g., specimens E20E-L06-45 and E25E-L06-45). Such local buckling typically occurred in the minor axis direction of the specimen, which is similar to the observation reported for concrete-filled elliptical steel tubes [26].

3.2. Axial stress-strain behaviour

Figure 9 shows the stress-strain curves of the confined concrete, and the key test results are summarized in Table 6. In Table 6, f'_{cu} and ε_{cu} are the axial stress and axial strain of concrete at the ultimate state when FRP rupture occurs; f'_{cc} is the peak stress of concrete, which is equal to f'_{cu} for sufficiently-confined concrete (for insufficiently confined-concrete $f'_{cu} < f'_{cc}$); ε_{hu} is the hoop rupture strain of FRP which is averaged from the readings of hoop strain gauges; $\varepsilon_{hu,max}$ is the maximum value among the hoop rupture strains recorded by all the hoop strain gauges in a specimen (see Figure 6). In this paper, the axial strain was calculated using the average readings of the four LVDTs covering the 240 mm mid-height region, unless otherwise specified. The axial stress was calculated by dividing the load taken by concrete by its cross-sectional area. The load taken by concrete was obtained by subtracting the total load on the column by the load taken by the FRP tube at the same strain. In these calculations, the test results of circular FRP rings under axial compression were used to calculate the load taken by the FRP tube in the column tests, with the following assumptions: (1) despite the variation of thickness among the elliptical tubes (Table 3), they have the same axial stress-strain curve as the corresponding circular tube; (2) for the FRP tubes with ±45° fibres, the stress-strain behaviour is linearly elastic before the peak stress, with the elastic modulus being equal to that obtained from the FRP ring compression tests (Table 5); (3) for the FRP tubes with ±80° fibres or ±60° fibres, the stress-strain behaviour is depicted by the curves shown in Figure 5 before the peak stress; (4) after the peak stress, the axial stress of the FRP tube decreases linearly with the axial strain and becomes zero at the ultimate state of the column. The last assumption is based on the test observation that significant axial damage of the FRP tube occurred before the final failure of the column. It is believed that these assumptions lead only to marginal errors considering the relatively small contribution made by the FRP tube to the axial resistance of the column.

Figures 9a-9d show the axial stress-strain curves of the specimens confined by an FRP tube with fibre orientations of ±80°. It is evident that only the specimens with a relatively small aspect ratio and/or a relatively low unconfined concrete strength show a monotonically ascending stress-strain response, while the other specimens may be classified as being insufficiently confined ($f'_{cu} < f'_{cc}$). It is also evident from Table 6 that the ultimate axial strain, ultimate hoop strain and the corresponding axial stress generally decrease with an increase in the aspect ratio, except for specimen E10B-L10-80 whose test was terminated before failure occurred. This is consistent with the findings of the previous studies [9, 11] on FRP-wrapped elliptical concrete specimens. As expected, an increase in the FRP thickness generally leads to an increase in the ultimate axial strain and the corresponding axial stress, but such increases appear to be less pronounced for the specimens with a relatively large aspect ratio (see Table 6). A similar observation was made by Campione and Fossetti [27] and Tan and Yip [28] for elliptical concrete columns with steel confinement.

For the specimens confined by an FRP tube with fibre orientations of ±60° and ±45°, Figures 9e and 9f show that the axial stress-strain curves do not exhibit a bilinear ascending shape, except that of specimen E10D-L06-60. This is not difficult to understand as these FRP tubes had a smaller hoop stiffness than the ±80° FRP tubes (see Table 4). It is also evident from Figures 9e and 9f that a larger aspect ratio leads to a lower curve, suggesting that the confinement effectiveness decreases with an increase in the aspect ratio. It should, however, be noted that the LVDTs became non-functional during the late stage of loading for the specimens with a ±45° FRP tube, due mainly to the excessive lateral expansion of these specimens. As a result, the curves shown in Figure 9f do not reflect the final stage of behaviour prior to the actual failure of these specimens, and their ultimate axial strains are thus unavailable. Similarly, the ultimate hoop strains of some specimens are also unavailable due to the premature damage of strain gauges (Table 6).

3.3. Hoop strain distribution

In FRP-confined elliptical columns, the concrete is subjected to non-uniform confinement. To understand the confinement mechanism, it is important to know the distribution of hoop strains around the circumference. In the present study, a number of hoop strain gauges were installed on each specimen, as shown in Figure 6. Figures 10-12 present the typical hoop strain distributions in the specimens of batches B, D and E, respectively. The hoop strain distributions of specimens in batch A and C are similar to those in batches B, D and E. Therefore, these results are not shown in this paper. In these figures, the vertical axis represents the hoop strain gauge reading, while the horizontal axis represents the central angle measured from one of the vertices on the major axis (i.e., major-axis vertices) of the elliptical section (i.e., the two vertices on the major axis correspond to central angles of 0° and 180° while those on the minor axis correspond to central angles of 90° and 270°). For each specimen, the hoop strain distributions are shown in two-line charts of a subfigure (e.g., Figure 10a) for two different axial strain levels, respectively. It is evident from the figures that for circular specimens (i.e., aspect ratio = 1.0), the hoop strain distributions do not change much in shape with the axial strain level. By contrast, for elliptical specimens, the hoop strain distributions appear to be quite different in shape at different axial strain levels, as elaborated below.

When the axial strain is relatively low (0.05%-0.35%), the hoop strains in the vicinities of the major-axis vertices are generally smaller than those in the vicinities of the minor-axis vertices and the difference appears to increase with the aspect ratio. This observation is consistent with that reported by Teng and Lam [9] and Teng et al. [11]. In addition, for the same axial strain, the hoop strain values of the specimens were found to increase as the angle of fibre orientations of the FRP tube decreased. This is believed to be due to the larger Poisson's ratio of an FRP tube with a smaller angle of fibre orientations. In the early stage of loading, the lateral expansion of concrete is relatively small, so the Poisson's effect due to the axial straining of FRP tubes contributes considerably to the hoop strain readings.

With increases in the axial strain, the hoop strain at/near one vertex or both vertices of the major axis increased rapidly and would likely become considerably higher than the hoop strains elsewhere (Figures 10-12). This observation is consistent with the failure modes as discussed above and is more evident for specimens with a larger aspect ratio. In addition, the maximum hoop strain measured at the rupture of FRP decreased with the aspect ratio, due largely to the increased curvature close to the major-axis vertices. It should be noted that the distributions of hoop strain in FRP-confined elliptical columns depend on many factors including the non-uniform dilation of concrete, the bending deformation of FRP tube, the local damage/cracking of concrete as well as the friction between FRP and concrete; the FRP tube itself must also satisfy force equilibrium in the hoop direction. The hoop strain distributions shown in Figures 10-12 depend on the combined effect of the above factors. A thorough understanding of this issue may be achieved through sophisticated three-dimensional finite element modelling which can be a topic of future study.

4. Performance of existing stress-strain models

To the best of the authors' knowledge, there are four existing design-oriented stress-strain models for FRP-confined concrete in elliptical columns. In this section, these four models are assessed using the test results of the present study. Only the results of batches A and B were used in the assessment, as the concrete in the elliptical specimens of other batches did not exhibit a bilinear ascending curve (i.e., not sufficiently confined).

4.1. Teng et al.'s [11] model

Teng et al.'s [11] model is based on a well-recognized model that was developed by the same research group for FRP-confined concrete in circular columns [15], which has been adopted in various design codes/guidelines [e.g., 17,29-30]. The two models [111,15] adopt the same set of equations as given below to depict the stress-strain curve:

$$\sigma_c = \begin{cases} E_c\varepsilon_c - \dfrac{\left(E_c - E_2\right)^2}{4f'_{co}}\varepsilon_c^2 & \left(0 \le \varepsilon_c < \varepsilon_t\right) \\ \begin{cases} f'_{co} + E_2\varepsilon_c & if\, \rho_K \ge 0.01 \\ f'_{co} & if\, \rho_K < 0.01 \end{cases} & \left(\varepsilon_t \le \varepsilon_c \le \varepsilon_{cu}\right) \end{cases} \tag{1}$$

$$E_2 = \frac{f'_{cc} - f'_{co}}{\varepsilon_{cu}} \tag{2}$$

$$\varepsilon_t = \frac{2f'_{co}}{E_c - E_2} \tag{3}$$

where σ_c is the axial stress; ε_c is the axial strain; E_c is the concrete elastic modulus; E_2 is the slope of the linear second portion; f'_{cc} is the compressive strength of confined concrete; f'_{co} is the compressive strength of unconfined concrete; ε_t is the transition strain between the parabolic first portion and the linear second portion; ε_{cu} is the axial strain of confined concrete at the ultimate state. The elastic modulus of unconfined concrete can be taken as $4730\sqrt{f'_{co}}$ (in MPa), following ACI 318-19 [31]. When $f'_{cc} = f'_{co}$ and ε_{cu} is taken as 0.0035, Eqs. 1-3 reduce to the stress-strain model in Concrete Society [30] for unconfined concrete.

In Teng et al.'s [15] model, the strength of confined concrete f'_{cc} and the ultimate axial strain ε_{cu} are determined by the confinement stiffness ratio ρ_K and strain ratio ρ_ε using the following equations:

$$\frac{f'_{cc}}{f'_{co}} = \begin{cases} 1+3.5(\rho_K - 0.01)\rho_\varepsilon & \text{if } \rho_K \geq 0.01 \\ 1 & \text{if } \rho_K < 0.01 \end{cases} \tag{4}$$

$$\frac{\varepsilon_{cu}}{\varepsilon_{co}} = 1.75 + 6.5\rho_K^{0.8}\rho_\varepsilon^{1.45} \tag{5}$$

$$\rho_K = \frac{2E_{FRP}t_f}{\left(f'_{co} / \varepsilon_{co}\right)D} \tag{6}$$

$$\rho_\varepsilon = \frac{\varepsilon_{hu,circular}}{\varepsilon_{co}} \tag{7}$$

where E_{FRP} is the hoop elastic modulus of FRP; t_f is the thickness of FRP tube; D is the inner diameter of circular FRP tube; $\varepsilon_{hu,circular}$ is the hoop rupture strain of circular column; ε_{co} is the strain at the compressive strength of unconfined concrete and is taken as 0.002. The confinement stiffness ratio, ρ_K, represents the confinement stiffness of the FRP relative to that of the concrete core. The strain ratio, ρ_ε, measures the strain capacity of the confining FRP relative to that of the concrete without confinement.

Apparently, the confinement stiffness ratio ρ_K (Eq.6) is only applicable to circular columns due to the use of the diameter D as a parameter. Therefore, Teng et al. [11] proposed that the confinement stiffness ratio ρ_K for elliptical columns can be calculated by replacing the term $2t_f / D$ in Eq. 6 with $\rho_{FRP} / 2$, where ρ_{FRP} is the FRP volumetric ratio. That is,

$$\rho_K = \frac{\rho_{FRP}E_{FRP}}{2}\frac{\varepsilon_{co}}{f'_{co}} \tag{8}$$

$$\rho_{FRP} = \frac{1.5(a+b) - \sqrt{ab}}{ab}t_f \tag{9}$$

In addition, Teng et al. [11] introduced a shape factor k_s to reflect the test observation that the hoop rupture strain of FRP in elliptical columns is lower than that in circular columns. That is,

$$\varepsilon_{hu} = k_s\varepsilon_{hu,circular} \tag{10}$$

$$k_s = 0.5\left(3 - \frac{a}{b}\right) \tag{11}$$

where *a* and *b* are the half lengths of major and minor axes, respectively.

Teng et al.'s [11] model suffers from two drawbacks. Firstly, the use of only the FRP volumetric ratio to determine the confinement stiffness ratio of FRP tubes appears to be oversimplified. In the experimental study presented above, the FRP volumetric ratio increases with the aspect ratio of the tube, but the test results evidently show that the confinement effectiveness decreases with the aspect ratio (Figure 9). Therefore, the predictions of Teng et al.'s [11] model are contradictory to the test results in terms of the effect of aspect ratio, as shown in Figure 13, although this model provides reasonably accurate predictions for circular columns (Figure 13).

The second drawback is associated with the determination of FRP rupture strain in elliptical columns. In Teng et al. [11], the equation for the shape factor (Eq. 10) was proposed based on a regression analysis of the limited test data reported in the same paper. However, the distribution of hoop strains in elliptical columns is highly non-uniform (see Figure 10), so the average hoop rupture strain obtained from a test depends significantly on the number and layout of the strain gauges. Therefore, the wide applicability of Eqs. 10 and 11 is uncertain.

4.2. Cao et al.'s [14] model

Cao et al. [14] developed a unified axial stress-strain model for FRP-confined concrete in circular, rectangular, square, and elliptical columns. The unique feature of their model is the use of an equivalent corner radius for elliptical columns. By doing so, the stress-strain curve of FRP-confined concrete in elliptical columns can be calculated based on that in rectangular columns with the same aspect ratio and corner radius. The equations of Cao et al.'s [14] model are not given here, but readers may refer to their paper for more details.

The predictions of Cao et al.'s [14] model are compared with the test results in Figure 14. While Cao et al.'s [14] model can predict the decrease of confinement effectiveness with the aspect ratio, there appears to be a significant discrepancy between the predictions and the test results, even for the circular specimens (Figure 14). In addition, the conversion of an elliptical column to a rectangular column in Cao et al.'s model [14] was purely on an empirical basis. As a result, their model suffers from its complex expressions, and its wide validity is in doubt. Cao et al.'s [14] model is not further discussed in this paper.

4.3. Stress-strain model in GB50608 [17]

In the latest version (i.e., second edition) of the Chinese national technical standard for the structural use of FRP composites in construction [17], a unified stress-strain model is provided for concrete sufficiently-confined by FRP in columns of various shapes (i.e., circular, rectangular, elliptical), with the effects of sectional shapes being accounted for by two coefficients $k_{s\sigma}$ and $k_{s\varepsilon}$ for the strength and the ultimate axial strain, respectively. The stress-strain model is basically based on Teng et al.'s [15] model, which adopts the two-branch stress-strain curve depicted by Eq. 1; the strength of confined concrete (f'_{cc}) and the ultimate compressive strain (ε_{cu}) are given by the following equations:

$$f'_{cc} = f'_{co} + 3.5\frac{E_{FRP}t_f}{R}\left(k_{s\sigma} - \frac{6.5}{\beta_j}\right)\varepsilon_{hu,circular} \tag{12}$$

$$\varepsilon_{cu} = 0.0033 + 0.6k_{s\varepsilon}\beta_j^{0.8}\varepsilon_{hu,circular}^{1.45} \tag{13}$$

$$\beta_{\mathrm{j}} = \frac{E_{FRP}t_f}{f'_{co}R} \tag{14}$$

where β_j is the confinement stiffness parameter; R is a geometric parameter, which is taken as the radius for circular sections and as the half length of the major axis for elliptical sections.

For circular sections, $k_{s\sigma}$ and $k_{s\varepsilon}$ are both taken as 1 and Eqs. 12-14 reduce to Eqs. 4-7 except for minor differences in the constants/coefficients. For elliptical columns, $k_{s\sigma}$ and $k_{s\varepsilon}$ are defined by the following two equations, respectively:

$$k_{s\sigma} = 1.6 - 0.6\left(\frac{a}{b}\right) \tag{15}$$

$$k_{s\varepsilon} = 1.3 - 0.3\left(\frac{a}{b}\right) \tag{16}$$

It should be noted that the GB50608 model was developed by the authors' group based largely on the test data of the present study. Similar to Teng et al.'s [11] model, the confinement stiffness of FRP is used in GB50608 [17] to decide whether the concrete is sufficiently confined (i.e., if $k_{s\sigma}\beta_j > 6.5$, the concrete is deemed to be sufficiently confined). By comparing Eq. 6 with Eq. 14, it is easy to see that this condition for sufficiently-confined concrete is similar to setting a lower limit for ρ_K; a simple calculation reveals that this condition is slightly stricter than setting a threshold of 0.01 for ρ_K (Eq. 4).

The predictions from the stress-strain model given in GB50608 [17] are compared with the experimental axial stress-strain curves of the present study in Figure 15. It can be seen that the GB50608 model generally provides reasonably accurate and conservative predictions. This is not a surprise as the test data of the present study were already used in developing the GB50608 model. Despite the good performance of the GB50608 model, it was formulated for predicting the section strength rather than the concrete stress-strain path as the main objective as was the case for Teng et al.'s [15] model. Indeed, in both models, the second-stage stiffness (i.e., E_2) is calculated using the stress and strain at the ultimate state (i.e., f'_{cc} and ε_{cu}) so that the predicted stress-strain path may be different for the same concrete confined with an FRP tube of the same confinement stiffness but a different rupture strain [16]. While this inaccuracy for the stress-strain path may not be a significant issue for member strength design based on the ultimate state, a more accurate stress-strain model is needed in advanced structural analysis (e.g., for seismic responses of columns) where the accurate prediction of stress-strain paths is important.

4.4. Chen et al.'s [12] model

Chen et al. [12] conducted a series of axial compression tests on FRP-confined high-strength concrete (f'_{co} =72.4 MPa) in elliptical columns and developed a new design-oriented stress-strain model. Chen et al. [12] adopted Teng et al.'s [15] expressions for circular columns as a framework of their model but developed new equations for the strength of confined concrete (f'_{cc}) and the ultimate axial strain (ε_{cu}). In this development, Chen et al. [12] made the following revisions to Teng et al.'s [15] original equations (i.e., Eqs. 4-7): (1) the use of an equivalent diameter (D_e) for calculating the confinement stiffness ratio ρ_K; and (2) the use of two additional shape factors (i.e., $k_{s\sigma}$ and $k_{s\varepsilon}$) for calculating f'_{cc} and the ultimate axial strain ε_{cu}, respectively.

With the first revision as mentioned above, Eq. 6 becomes:

$$\rho_K = \frac{2E_{FRP}t_f}{\left(f'_{co} / \varepsilon_{co}\right)D_e} \tag{17}$$

where

$$D_e = \frac{2a^2}{b} \tag{18}$$

With the second revision as mentioned above, Eqs. 4 and 5 become:

$$\frac{f'_{cc}}{f'_{co}} = \begin{cases} 1 + 3.5k_{s\sigma}\left(\rho_K - 0.01\right)\rho_\varepsilon & \text{if } \rho_K \geq 0.01 \\ 1 & \text{if } \rho_K < 0.01 \end{cases} \tag{19}$$

and

$$\frac{\varepsilon_{cu}}{\varepsilon_{co}} = 1.75 + 6.5k_{s\varepsilon}\rho_K^{0.8}\rho_\varepsilon^{1.45} \tag{20}$$

where

$$k_{s\sigma} = 1 \tag{21}$$

$$k_{s\varepsilon} = \left(\frac{a}{b}\right)^{-0.25} \tag{22}$$

It is worth noting that Chen et al.'s [12] model adopts the hoop rupture strain of FRP in circular columns ($\varepsilon_{hu,circular}$) to calculate the strain ratio (ρ_ε) of elliptical columns (i.e., Eq. 7).

Chen et al.'s [12] model appears to work well for the test results presented in their paper in terms of the strength and the ultimate axial strain of the confined concrete. However, similar to Teng et al.'s [15] model, it suffers from inaccuracy in predicting the stress-strain path as discussed above. Furthermore, in Chen et al.'s [12] model, the calculation of the confinement stiffness ratio ρ_K is based on an equivalent diameter (D_e) (Eq. 18) which was derived largely from qualitative observations instead of rigorous calibration with their test results. As a result, the so-obtained ρ_K generally overestimates the second-stage stiffness of the relatively weakly-confined concrete in the present study (e.g., specimen E20B-L06-80, see Figure 16).

5. New stiffness-based stress-strain model

To provide accurate predictions for the stress-strain path of confined concrete in EFCCCs, a so-called stiffness-based stress-strain model for EFCCCs was developed in the present study following the approach of Lin et al. [16]. This approach is based on the widely-accepted conclusion that the second-stage stiffness of the stress-strain curve of FRP-confined concrete (i.e., E_2) depends on the confinement stiffness rather than the rupture strain of the FRP confining jacket/tube [15, 32-35].

Compared with the existing models, the new model includes a more rigorous treatment of the confinement stiffness for EFCCCs based mainly on the test results of sufficiently-confined concrete (i.e., $f'_{cc}=f'_{cu}$) in batches A and B of the present study; in this process, the equivalent confinement stiffness ratio ρ_{Ke} is directly calibrated using the test results of E_2. The new model is then verified against the test results from previous studies, including those presented in Teng et al. [11] and Chen et al. [12]. In this section, the development of the new model and its performance evaluation are presented.

5.1. Proposed model

Lin et al. [16] proposed the following equation to relate ρ_K and E_2 of FRP-confined concrete in circular columns based on a systematic parametric study using the well-known analysis-oriented model proposed by Jiang and Teng [36]:

$$\frac{E_2}{f'_{co}} = 29.9\ln\left(\rho_K\right) + 134 \tag{23}$$

In the present study, an equivalent confinement stiffness ratio ρ_{Ke} is proposed for elliptical columns, which is calibrated using Eq. 23 and the present test results of EFCCCs. That is,

$$\frac{E_2}{f'_{co}} = 29.9\ln\left(\rho_{Ke}\right) + 134 \tag{24}$$

$$\rho_{Ke} = k_k \rho_K \tag{25}$$

where k_k is the modification factor for the equivalent confinement stiffness ratio of EFCCCs.

For the present purpose, the confinement stiffness ratio ρ_K for EFCCCs is defined by Eq. 6, except that D is replaced with an equivalent diameter, D_e, and D_e is simply taken as the length of the major axis (i.e., $2a$). It should be noted that this choice of D_e is primarily for ease of calculation since its actual form is not greatly important; instead, the modification factor k_k is relied upon and calibrated with the present test results to achieve an accurate definition of the equivalent confinement stiffness ratio.

In the calibration process, the test results of E_2 for those specimens with $f'_{cc} = f'_{cu}$ in batches A and B were used (see Table 7), which were found from by Eq. 2 using the test values of f'_{cc} and ε_{cu}. The correlation between k_k and the aspect ratio (a/b) is illustrated in Figure 17. To strike a good balance between the complexity and performance of the confinement stiffness ratio equation, it is proposed that the factor k_k be a parabolic function of the aspect ratio a/b, leading to the following equation which ensures that ρ_{Ke} can be reduced to ρ_K for circular columns (i.e., $k_k = 1$ when $a/b = 1$):

$$k_k = 0.095 \times \left(\frac{a}{b}\right)^2 - 0.860 \times \left(\frac{a}{b}\right) + 1.765 \tag{26}$$

It is further proposed that an independent shape factor (i.e., k_ε) be introduced for the evaluation of ε_{cu}. As a result, Eq. 5 becomes:

$$\frac{\varepsilon_{cu}}{\varepsilon_{co}} = 1.75 + 6.5 k_\varepsilon \rho_{Ke}^{0.8} \rho_\varepsilon^{1.45} \tag{27}$$

In Eq. 27, the hoop rupture strain of FRP in circular columns ($\varepsilon_{hu,circular}$) is simply adopted for calculating ρ_ε due to difficulties with defining/measuring FRP rupture strains in elliptical columns as the FRP hoop strain varies around the column perimeter in a pattern that is determined by the section aspect ratio. The effect of differences between elliptical and circular columns in the FRP rupture strain on ε_{cu} are implicitly accounted for by the shape factor k_ε.

The k_ε values were first back-calculated using Eq. 27 and the test results for specimens with $f'_{cc} = f'_{cu}$. In doing so, the values of strain ratio ρ_ε of the test specimens were calculated using the average value (i.e., 0.0192) of the hoop rupture strains of the two circular specimens of batches A and B (i.e., specimens E10A-L06-80 and E10B-L06-80). The so-obtained k_ε values are shown against the aspect ratio (a/b) in Figure 18. The k_ε value appears to increase with the aspect ratio, except for specimen E20B-L10-80, whose k_ε value is unusually low. Further examination of the test results revealed that the ultimate axial strain of specimen E20B-L10-80 with a 10-layer GFRP tube is even lower than those of the two specimens with a thinner (6-layer) tube (Table 6), so this specimen (i.e., E20B-L10-80) was deemed to be an outlier and was not considered in developing the model. It is also noted that the k_ε values of the two circular specimens (i.e., $a/b = 1$) are considerably lower than one. This could be due to the scatter of the test results. In addition, the ρ_ε value used in the back-calculation of k_ε can significantly affect the results. To further examine this issue, the two hoop rupture strains (i.e., 0.0179 and 0.0204) obtained respectively from the two circular specimens (i.e., specimens E10A-L06-80 and E10B-L06-80) were also used separately to back-calculate the k_ε values, and the results for all the specimens are also shown in Figure 18. It is evident that k_ε generally increases with the aspect ratio despite the scatter of results. By observing the test data in Figure 18, the following equation, which ensures that k_ε is equal to unity for circular columns, is proposed for k_ε:

$$k_\varepsilon = 0.19\left(\frac{a}{b}\right) + 0.81 \tag{28}$$

Once the values of E_2 and ε_{cu} are known, the strength of confined concrete f'_{cc} can be calculated using Eq. 2 instead of Eq. 4, while the stress-strain curve can be determined by a slightly revised version of Eq. 1:

$$\sigma_c = \begin{cases} E_c\varepsilon_c - \dfrac{\left(E_c - E_2\right)^2}{4f'_{co}}\varepsilon_c^2 & \left(0 \le \varepsilon_c < \varepsilon_t\right) \\ f'_{co} + E_2\varepsilon_c \quad if\, \rho_{Ke} \ge 0.0113 & \left(\varepsilon_t \le \varepsilon_c \le \varepsilon_{cu}\right) \end{cases} \tag{29}$$

It is evident that the main differences between Eq. 29 and Eq. 1 are that: (1) ρ_K is replaced by ρ_{Ke} for EFCCCs; (2) the threshold value of ρ_{Ke} for sufficiently-confined concrete is slightly changed from 0.01 to 0.0113. The slight change in the threshold value is to ensure that E_2 is larger than zero according to Lin et al.'s [16] equation (Eq. 23).

In summary, the proposed model consists of Eqs. 3, 24 & 29 for the stress-strain curve, and Eq. 27 for ε_{cu}; in these equations, ρ_{Ke} is defined by Eqs. 25 & 26, and k_ε is obtained from Eq. 28, while ρ_ε is taken to be the same as that for the corresponding circular column (i.e., Eq. 7). E_c is taken as $4730\sqrt{f'_{co}}$ and ε_{co} is taken as 0.002.

It should be noted that the proposed model as summarized above is based only on the test results of sufficiently-confined concrete ($f'_{cc} = f'_{cu}$). For EFCCCs with $f'_{cu} < f'_{cc}$, the concrete generally experiences a drop in stress soon after the unconfined concrete strength is reached. While the ductility of concrete in elliptical columns may still be improved by FRP confinement, the limited test results with a considerable scatter do not allow a reliable design equation to be established for such insufficiently-confined concrete. Therefore, it is recommended that for insufficiently-confined concrete in EFCCCs ($f'_{cu} < f'_{cc}$), the stress-strain curve of unconfined concrete should be adopted for conservative use in design; in such cases, Eqs. 1-3 may be used with $f'_{cc} = f'_{co}$ and $\varepsilon_{cu} = 0.0035$.

5.2. Performance of the proposed model

The predictions of the new stress-strain model are compared with the experimental axial stress-strain curves in Figure 19 for all the specimens of batches A and B with $f'_{cc} = f'_{cu}$. In making the predictions for all the specimens, the average rupture strain (i.e., 0.0192) of the two circular test specimens was used to calculate the strain ratio. It is evident that in general, the performance of the proposed model is significantly better than that of the existing models in terms of the stress-strain paths, particularly for the second linear portion (see Figures 13-16). The only exception is for specimen E25B-L10-80 which is conservatively predicted to be insufficiently confined by the new model while in reality its experimental f'_{cu} is slightly higher than the stress at the transition point of the stress-strain curve. This is not a surprise as Eq. 26 slightly underestimates the experimental k_k of the specimen (see Figure 17). Nevertheless, considering that specimen E25B-L10-80 is the only "sufficiently-confined" specimen of all the existing studies with a large aspect ratio of 2.5, it is believed that the conservative treatment of k_k using Eq. 26 is appropriate for the moment.

In Figure 20, the predicted and the experimental values for E_2, f'_{cc} and ε_{cu} are compared for the specimens of the present study and those reported in Teng et al. [11] and Chen et al. [12], while the details including the experimental $\varepsilon_{hu,circular}$ values are given in Tables 8 and 9. It is evident that the proposed model provides reasonably accurate predictions for f'_{cc} and ε_{cu}. It is also noted that Eqs. 24-26 appear to slightly underestimate E_2, especially for the specimens in Teng et al. [11]. This is due to the use of only the test results of the present study for calibrating k_k. To further examine this issue, the test k_k values of the specimens in Teng et al. [11], Chen et al. [12] and the present study are plotted together against the predictions of Eq. 26 in Figure 21. It is evident that there is a large scatter of the test results, while the proposed equation (Eq. 21) generally provides conservative predictions. A possible way to improve the accuracy of predictions is to find the best-fit equation for k_k using all the test data points in Figure 21, but by doing so, it is unlikely that the resulting ρ_{Ke} equation can be reduced to ρ_K for circular columns (i.e., $k_k = 1$ for circular columns), given that the majority of the test data points in Figure 21 [mainly those in Teng et al., [11]] indicate values significantly higher than 1 at the aspect ratio of 1. Considering the large scatter of the test results (Figure 21) and the fact that Eq. 23 was calibrated from a systematic parametric study based on the well-established Jiang and Teng's [36] analysis-oriented model and has been verified against a much larger database for circular columns [16], it is believed that it is most appropriate to use Eq. 26 for k_k which leads to conservative predictions for E_2 (Figure 20a) and reasonably accurate predictions for f'_{cc} and ε_{cu} (Figure 20b and 20c).

Because of its improved accuracy, the new model is more suitable than the model in GB50608 [17] for use in advanced analysis where the correct prediction of deformation is of critical importance (e.g., for seismic responses of columns). Nevertheless, the model given in GB50608 [17], which adopts simple expressions for key parameters and a direct equation for the strength of confined concrete (Eq. 12), is still more suitable for convenient design use. This is also supported by Figure 22, which further illustrates that the GB50608 model, while being less accurate than the proposed new model, generally provides conservative and reasonably close predictions for the experimental f'_{cc} and ε_{cu} values of the present specimens and those of Teng et al. [11] and Chen et al. [12].

6. Conclusions

This paper has presented an experimental study involving axial compression tests on elliptical concrete columns confined with a filament-wound FRP tube. The test variables covered include the section aspect ratio and the concrete strength, as well as the thickness and fibre orientations of the FRP tube. The following conclusions may be drawn from the study:

1. The circumferential elastic modulus of elliptical filament-wound FRP tubes is little affected by its aspect ratio.
2. The confinement effectiveness of the FRP tube on the concrete core decreases as the aspect ratio or the concrete strength increases, but increases with the FRP tube thickness.
3. The orientations of fibres in the FRP tube directly affect its confinement effectiveness and the failure mode of EFCCCs. For the specimens with ±45° fibre orientations, failure appears to be a gradual process instead of explosive fibre rupture.
4. The hoop strain distribution in an elliptical FRP tube in a confined column is highly non-uniform. At the ultimate state, the maximum hoop strain generally occurs at or near one of the vertices (i.e., ends of the major axis).

Furthermore, a new stiffness-based stress-strain model has been proposed for FRP-confined concrete in EFCCCs, which includes a more rigorous treatment of the confinement stiffness of EFCCCs. This new model has been found to closely predict the available test results of EFCCCs.

Acknowledgements

The authors are grateful for the financial support received from the National Key R&D Program of China (Project No.: 2017YFC0703000) and the Hong Kong Research Grants Council (Project Nos: PolyU 152217/15E and T22-502/18-R). The experimental study was conducted at Guangdong University of Technology (GDUT). The authors are grateful for the support received from Dr Guang-Ming Chen, Dr Bing Fu, Dr Yong-Chang Guo, Mr Xiao-Dong Mo, Dr Xue-Fei Nie, Mr Zhen-Xiong Wang, Dr. Pan Xie and Dr Gen-Quan Zhong in the experimental work. The authors are also grateful to Dr Guan Lin who contributed to the development of the model in GB50608 [17] and provided valuable discussions in the preparation of the paper.

References

[1] Chan T.M., Gardner L. and Law K.H. Structural design of elliptical hollow sections: A review. *Proceedings of ICE-Structures and Buildings* 2010; *163*: 391-402.

[2] Zhao X.L., Packer J.A. Tests and design of concrete-filled elliptical hollow section stub columns. *Thin-Walled Structures* 2009; 47(6-7): 617-628.

[3] Lam D., Gardner L. and Burdett M. Behaviour of axially loaded concrete filled stainless steel elliptical stub columns. *Advances in Structural Engineering* 2010; 13(3): 493-500.

[4] Sheehan T., Dai X.H., Chan T.M. and Lam D. Structural response of concrete-filled elliptical steel hollow sections under eccentric compression. *Engineering Structures* 2012; 45:314-323.

[5] Liu F., Wang Y. andChan T.M. Behaviour of concrete-filled cold-formed elliptical hollow sections with varying aspect ratios. *Thin-Walled Structures* 2017; 110: 47-61.

[6] Xu Y., Yao J. and Sun X. Cold-formed elliptical concrete-filled steel tubular columns subjected to monotonic and cyclic axial compression. *Advances in Structural Engineering* 2020; 23(7): 1383-1396.

[7] Liao J., Li Y.L., Ouyang Y. and Zeng J.J. Axial compression tests on elliptical high strength steel tubes filled with self-compacting concrete of different mix proportions. *Journal of Building Engineering* 2021; 40: 102678.

[8] Liu K.C., Jiang C., Yu T. and Teng J.G. Axial compression tests on elliptical FRP tube-confined concrete columns [extended abstract], *Proceedings, Seventh Asia-Pacific Conference on FRP in Structures (APFIS 2019)*, 10-13 December, Surfers Paradise, Gold Coast, Australia.

[9] Teng J.G., Lam L. Compressive behaviour of carbon fiber reinforced polymer-confined concrete in elliptical columns. *Journal of Structural Engineering* 2002; 128(12): 1535-1545.

[10] Yan Z., Pantelides C.P. and Reaveley L.D. Fiber-reinforced polymer jacketed and shape-modified compression members: I-Experimental behaviour. *ACI Structural Journal* 2006; 103(6): 885-893.

[11] Teng J.G., Wu J.Y., Casalboni S., Xiao Q.G., Zhao Y. Behaviour and modeling of fiber-reinforced polymer-confined concrete in elliptical columns. *Advances in Structural Engineering* 2016; 19(9): 1359-1378.

[12] Chen G.P., Wang Y.L., Yu T., Wan B.L., Zhang B. and Liu Q. Behavior and design-oriented model for elliptical FRP-confined concrete under axial compression. *Engineering Structures* 2021; 249: 113387.

[13] Zhang B., Feng G., Wei W., Zhang N., Zhang Q. and Hu X. Effect of the long-axis and short-axis ratio on the axial compressive behavior of elliptical GFRP-confined concrete. Journal of Nanjing Tech University (Natural Science Edition) 2021; 43:80-6 [in Chinese].

[14] Cao Y.G., Jiang C. and Wu, Y.F. Cross-sectional unification on the stress-strain model of concrete subjected to high passive confinement by fiber-reinforced polymer. *Polymers* 2016; 8(5): 186.

[15] Teng J.G., Jiang T., Lam L., Luo Y.Z. Refinement of a design-oriented stress-strain model for FRP-confined concrete. *Journal of Composites for Construction* 2009; 13(4): 269-278.

[16] Lin G., Yu T. and Teng, J.G. Design-oriented stress–strain model for concrete under combined FRP-steel confinement. *Journal of Composites for Construction* 2016; 20(4): 04015084.

[17] GB 50608. *Technical standard for fiber reinforced polymer (FRP) in construction.* China Planning Press, Beijing 2020.

[18] ASTM C39. *Standard test method for compressive strength of cylindrical concrete specimens*. West Conshohocken, PA, USA 2016.

[19] ASTM C469. *Standard test method for static modulus of elasticity and Poisson's ratio of concrete in compression*. West Conshohocken, PA, USA 2014.

[20] Teng J.G., Xie P., Wang Z.H. andLiu K.C. A novel test method for the determination of hoop elastic modulus and Poisson's ratio of FRP tubes. Chinese Patent filed on 6 April 2021, Patent Application Number: 202110366444.7.

[21] Teng J.G., Wang Z.H., Yu T., Zhao Y., Li L.J. Double-tube concrete columns with a high-strength internal steel tube: Concept and behaviour under axial compression. *Advances in Structural Engineering* 2018; 21(10): 1585-1594.

[22] Zhou J.K., Lin G. and Teng J.G. Compound concrete-filled FRP tubular columns under cyclic axial compression. *Composite Structures* 2021; 275: 114329.

[23] ASTM D2290. *Standard test method for apparent tensile strength of plastic or reinforced plastic pipe by split disk method*. West Conshohocken, PA, USA 2019.

[24] Zhang, B., Hu, X.M., Zhao, Q., Huang, T., Zhang, N.Y. and Zhang, Q. B. Effect of fiber angles on normal-and high-strength concrete-filled fiber-reinforced polymer tubes under monotonic axial compression. *Advances in Structural Engineering* 2020; 23(5): 924-940.

[25] GB/T 5350. *Fiber-reinforced thermosetting plastic composites pipe-determination for longitudinal compressive properties*. Standardization Administration of the PRC, Beijing 2005.

[26] Uenaka K. Experimental study on concrete filled elliptical/oval steel tubular stub columns under compression. *Thin-Walled Structures* 2014; 78: 131-137.

[27] Campione G., Fossetti M. Compressive behaviour of concrete elliptical columns confined by single hoops. *Engineering Structures* 2007; 29(3): 408-417.

[28] Tan T.H., Yip W.K. Behaviour of axially loaded concrete columns confined by elliptical hoops. *ACI Structural Journal* 1999; 96(6): 967-971.

[29] ACI 440.2R-17. *Guide for the design and construction of externally bonded FRP systems for strengthening concrete structures*. Farmington Hills, MI, USA 2017.

[30] Concrete Society. *Design Guidance for Strengthening Concrete Structures Using Fibre Composite Materials* (Technical Report no. 55). 3rd ed. Crowthorne: Concrete Society 2012.

[31] ACI 318-19. *Building code requirements for structural concrete and commentary*. Farmington Hills, MI, USA 2019.

[32] Binici, B. Design of FRPs in circular bridge column retrofits for ductility enhancement. *Engineering Structures* 2008; 30(3): 766-776.

[33] Jesus M., Lobo P.S. and Faustino P. Design models for circular and square RC columns confined with GFRP sheets under axial compression. *Composites Part B: Engineering* 2018; 141: 60-69.

[34] Karbhari V.M., Gao Y. Composite jacketed concrete under uniaxial compression – Verification of simple design equations. *Journal of Materials in Civil Engineering* 1997; 9(4): 185-193.

[35] Youssef M.N., Feng M.Q. and Mosallam A.S. Stress–strain model for concrete confined by FRP composites. *Composites Part B: Engineering* 2007; 38(5-6): 614-628.

[36] Jiang T., Teng J.G. Analysis-oriented stress–strain models for FRP–confined concrete. *Engineering Structures* 2007; 29(11): 2968-2986.

Tables

Table 1. Details of specimens

Batch	Specimen	Nominal aspect ratio	Height (mm)	Fibre orientations of FRP tube	Number of fibre layers in FRP tube	Concrete properties			
						Compressive strength f'_{co} (MPa)	Axial strain ε_{co} (%) at f'_{co}	Young's modulus E_c (GPa)	Poisson's ratio v
A	E10A-L06-80	1	600	±80°	6	41.2	0.213	34.2	0.185
	E15A-L06-80	1.5							
	E20A-L06-80	2.0							
	E25A-L06-80	2.5							
B	E10B-L06-80	1			6	53.6	0.263	32.0	0.192
	E10B-L10-80				10				
	E15B-L06-80	1.5			6				
	E15B-L10-80				10				
	E20B-L06-80	2.0			6				
	E20B-L10-80				10				
	E25B-L06-80	2.5			6				
	E25B-L10-80				10				
C	E10C-L06-80	1			6	75.7	0.262	38.6	0.196
	E15C-L06-80	1.5							
	E20C-L06-80	2.0							
	E25C-L06-80	2.5							
D	E10D-L06-60	1		±60°		55.9	0.271	32.5	0.208
	E15D-L06-60	1.5							
	E20D-L06-60	2.0							
	E25D-L06-60	2.5							
E	E10E-L06-45	1		±45°		55.1	0.269	32.3	0.198
	E15E-L06-45	1.5							
	E20E-L06-45	2.0							
	E25E-L06-45	2.5							

Table 2. Mix proportions of concrete

	Coarse aggregate (kg/m^3)	Fine aggregate (kg/m^3)	Cement (kg/m^3)	Water (kg/m^3)	Water reducer (kg/m^3)
Batch A	1072	760	343	175	N.A.
Batches B, D & E	1089	667	471	223	N.A.
Batch C	1023	689	506	177	3.04

Table 3. Dimensions of GFRP tubes

Nominal Aspect ratio	Major axis length, 2*a* (mm)	Minor axis length, 2*b* (mm)
1.0	299.5	299.5
1.5	295.9	196.0
2.0	297.9	150.3
2.5	295.8	119.4

Nominal aspect ratio/number of fibre layers/fibre orientations	Average tube thickness (mm)
1.0 / 6 / ±80°	2.89
1.5 / 6 / ±80°	2.84
2.0 / 6 / ±80°	3.14
2.5 / 6 / ±80°	3.15
1.0 / 10 / ±80°	4.85
1.5 / 10 / ±80°	4.43
2.0 / 10 / ±80°	4.26
2.5 / 10 / ±80°	4.41
1.0 / 6 / ±60°	3.27
1.5 / 6 / ±60°	3.38
2.0 / 6 / ±60°	2.72
2.5 / 6 / ±60°	2.89
1.0 / 6 / ±45°	3.76
1.5 / 6 / ±45°	4.05
2.0 / 6 / ±45°	4.01
2.5 / 6 / ±45°	3.76

Table 4. Key results of curved coupon tests

Fibre Orientations – ±80°

Specimen*	No.	Thickness t_f (mm)	Width (mm)	E_t (GPa)	Average E_t (GPa)	$E_t \times t_f$	Average $E_t \times t_f$	Specimen*	No.	Thickness t_f (mm)	Width (mm)	E_t (GPa)	Average E_t (GPa)	$E_t \times t_f$	Average $E_t \times t_f$
A15FO80L06	I	3.27	30.8	39.9	40.8	130.5	127.1	A15FO80L10	I	4.64	32.0	39.5	39.5	183.0	183.4
	II	3.14	30.3	40.0		125.6			II	4.64	32.0	39.4		182.6	
	III	3.00	31.2	39.3		117.9			III	4.57	29.9	39.4		180.2	
	IV	3.02	29.1	43.0		129.9			IV	4.72	31.1	39.7		187.5	
	V	3.11	31.1	41.7		129.7			V	4.71	29.8	N.A.		N.A.	
A20FO80L06	I	3.48	31.5	35.2	37.5	122.5	122.3	A20FO80L10	I	4.69	28.7	41.6	40.7	195.2	190.7
	II	3.22	31.7	37.4		120.4			II	4.91	29.7	37.6		184.6	
	III	3.06	31.3	39.2		120.0			III	4.67	31.4	N.A.		N.A.	
	IV	3.32	31.7	38.0		126.2			IV	4.68	30.4	42.9		200.8	
	V	3.37	31.2	N.A.		N.A.			V	4.48	33.1	40.7		182.2	
A25FO80L06	I	3.75	30.5	35.4	35.9	132.7	127.5	A25FO80L10	I	4.70	32.0	39.7	39.5	186.5	186.3
	II	3.30	31.1	36.9		121.7			II	4.70	29.7	39.6		186.2	
	III	3.75	30.5	34.9		130.8			III	4.90	30.6	40.5		198.6	
	IV	3.45	31.7	37.0		127.6			IV	4.70	31.4	39.6		185.9	
	V	3.53	30.9	35.2		124.1			V	4.59	31.8	38.0		174.4	

Fibre Orientations - ±60°

Specimen*	No.	Thickness (mm)	Width (mm)	E_t (GPa)	Thickness (mm)	Average E_t (GPa)
A15FO60L06	I	3.10	30.6	15.9	3.04	15.6
	II	3.15	29.3	16.3		
	III	2.97	30.5	14.5		
	IV	2.86	30.8	15.1		
	V	3.13	29.8	16.2		

Fibre Orientations - ±45°

Specimen*	No.	Thickness (mm)	Width (mm)	E_t (GPa)	Thickness (mm)	Average E_t (GPa)
A15FO45L06	I	3.41	30.2	8.51	3.82	8.92
	II	4.23	32.1	7.90		
	III	3.72	30.3	10.11		
	IV	4.01	31.0	7.90		
	V	3.75	30.8	10.11		

Note: *The specimen name includes the following components: (1) "A" plus a two-digit number representing the aspect ratio of the parent tube for the curved coupon (e.g. A15 for an aspect ratio of 1.5); (2) "FO" plus a two-digit number representing the fibre orientations; (3) "L" plus a two-digit number representing the number of fibre layers in the coupon.

Table 5. Key results of FRP rings under axial compression

Specimen*	Thickness t_f (mm)	Height H (mm)	Diameter D (mm)	Axial elastic modulus E_a (GPa)	Average E_a	Peak stress σ_{peak}	Average σ_{peak}	Poisson's ratio v_{12}	Average v_{12}
FO-80-1	2.80	58.2	299.5	10.1	10.6	69.5	70.5	0.097	0.093
FO-80-2	2.83	59.6		11.0		68.7		0.098	
FO-80-3	2.86	59.6		10.9		73.3		0.083	
FO-60-1	3.46	63.1		15.6	14.9	66.2	68.9	0.468	0.470
FO-60-2	3.37	61.3		14.3		70.4		0.484	
FO-60-3	3.43	60.2		14.9		70.2		0.459	
FO-45-1	3.80	62.5		30.5	31.6	85.6	86.2	1.161	1.110
FO-45-2	3.82	61.2		33.4		92.6		0.989	
FO-45-3	3.80	61.8		30.8		80.4		1.187	

Note: *The specimen name (FO-XX-Y): FO - fibre orientations; XX - fibre orientation angle (in degrees); Y – indicator to differentiate nominally identical specimens.

Table 6. Key test results of EFCCC specimens

Specimen	f'_{cu} (MPa)	f'_{cu}/f'_{co}	Ultimate axial strain ε_{cu} (%)	$\varepsilon_{cu}/\varepsilon_{co}$	f'_{cc} (MPa)	ε_{cc} (%)	Ultimate hoop strain ε_{hu} (%)	Maximum hoop strain $\varepsilon_{hu,max}$ (%)	Strain gauge recording $\varepsilon_{hu,max}^{\#}$
E10A-L06-80	85.6	2.08	2.73	12.82	85.6	2.73	1.79	1.82	H2
E15A-L06-80	73.4	1.78	2.44	11.46	73.4	2.44	1.34	1.65	H9
E20A-L06-80	52.0	1.26	1.99	9.34	52.0	1.99	0.87	1.54	H11
E25A-L06-80	43.7	1.06	2.15	10.8	43.8	0.39	0.65	1.41	H11
E10B-L06-80	89.8	1.68	2.19	8.33	89.8	2.19	2.04	2.13	H3
E10B-L10-80	112.2*	2.09*	2.41*	7.98*	112.2*	2.41*	1.41^{*}	1.56*	H7
E15B-L06-80	77.2	1.44	2.06	7.83	77.2	2.06	1.51	2.04	H5
E15B-L10-80	102.5	1.91	2.56	9.73	102.5	2.56	1.53	1.82	H8
E20B-L06-80	57.2	1.07	1.66	6.31	57.2	1.66	1.05	1.49	H2
E20B-L10-80	66.5	1.24	1.58	6.01	66.5	1.58	1.06	1.39	H12
E25B-L06-80	50.5	0.94	1.49	5.67	52.0	0.47	0.79	1.24	H12
E25B-L10-80	60.3	1.13	1.48	5.63	60.3	1.13	0.60	1.10	H6
E10C-L06-80	95.9	1.27	0.84	3.21	95.9	0.84	-	-	-
E15C-L06-80	74.5	0.98	1.02	3.85	80.0	0.43	-	-	-
E20C-L06-80	55.1	0.73	0.96	3.66	79.2	0.32	-	-	-
E25C-L06-80	55.3	0.73	0.86	3.28	84.0	0.35	-	-	-
E10D-L06-60	61.6	1.10	1.54	5.68	61.6	1.54	2.05	2.70	H6
E15D-L06-60	51.4	0.92	1.26	4.65	51.4	0.92	1.15	1.61	H11
E20D-L06-60	36.0	0.64	1.54	5.68	44.7	0.41	-	-	-
E25D-L06-60	33.0	0.59	1.30	4.80	47.4	0.34	0.77	1.76	H9
E10E-L06-45	24.2	0.44	4.00	14.87	41.7	0.26	-	-	-
E15E-L06-45	22.3	0.40	3.80	14.13	42.8	0.28	-	-	-
E20E-L06-45	19.3	0.35	2.56	9.52	41.4	0.27	-	-	-
E25E-L06-45	17.0	0.31	3.20	11.90	39.8	0.24	-	-	-

Note: - = results not available due to damaged strain gauges or LVDTs; * = value at the end of the test when the test was terminated due to the limitation of the machine's load capacity; $^{\#}$ = strain gauge identifier as defined in Figure 6.

Table 7. Test results of E_2

Specimen	f'_{co} (MPa)	f'_{cc} (MPa)	ε_{cu} (%)	E_2
E10A-L06-80	41.2	85.6	2.73	1626
E15A-L06-80		73.4	2.44	1312
E20A-L06-80		52.0	1.99	542.7
E10B-L06-80	53.6	89.8	2.19	1654
E15B-L06-80		77.2	2.06	1147
E20B-L06-80		57.2	1.66	218.1
E10B-L10-80		112.2*	2.41*	2432
E15B-L10-80		102.5	2.56	1911
E20B-L10-80		66.5	1.58	817.7
E25B-L10-80		60.3	1.48	454.1

Note: *= value at the end of the test when the test was terminated due to the limitation of the machine's load capacity

Table 8. Performance of the proposed model against the test results of the present study

	Specimen	$\varepsilon_{hu,circular}$ (%)	f'_{cc} (MPa)	Predicted f'_{cc} (MPa)	$f'_{cc,pre}/f'_{cc,exp}$	ε_{cu} (%)	Predicted ε_{cu} (%)	$\varepsilon_{cu,pre}/\varepsilon_{cu,exp}$
Present study	E10A-L06-80	1.92	85.6	88.7	1.04	2.73	3.01	1.10
	E15A-L06-80		73.4	69.5	0.95	2.44	2.52	1.03
	E20A-L06-80		52.0	52.2	1.00	1.99	1.97	0.99
	E10B-L06-80		89.8	94.4	1.05	2.19	2.50	1.14
	E15B-L06-80		77.2	75.5	0.98	2.06	2.08	1.01
	E20B-L06-80		57.2	58.6	1.02	1.66	1.67	1.00
	E15B-L10-80		102.5	99.8	0.97	2.56	2.76	1.08
	E20B-L10-80		66.5	73.7	1.11	1.58	2.16	1.36
	E25B-L10-80		60.3	53.6*	0.89	1.48	0.35	0.24*
				Average	**1.00**			**1.00**

Note: *= The specimen is classified as insufficiently-confined, so its stress-strain behaviour is assumed to be the same as that of unconfined concrete (i.e., Eqs. 1-3 with $f'_{cc} = f'_{co}$ and $\varepsilon_{cu} = 0.0035$)

.

Table 9 (part I). Performance of the proposed model against the test results of Ref. [11]

	Specimen	$2a$ (mm)	$2b$ (mm)	f'_{co} (MPa)	E_t (GPa)	t_f (mm)	$\varepsilon_{hu,circular}$ (%)	Experimental f'_{cc} (MPa)	Predicted f'_{cc} (MPa)	$f'_{cc,pre}/f'_{cc,exp}$	Experimental ε_{cu} (%)	Predicted ε_{cu} (%)	$\varepsilon_{cu,pre}/\varepsilon_{cu,exp}$
Ref. [11]	E10-A-I	200.4	200.4	32.6	242	0.17	0.82	43.4	39.5	0.91	0.78	0.88	1.12
	E10-A-II	199.7	199.7					43.5	39.6	0.91	0.87	0.88	1.01
	E13-A-I	202.8	155.9					42.9	37.2	0.87	0.82	0.82	1.00
	E13-A-II	201.0	154.7					40.2	37.3	0.93	0.74	0.82	1.10
	E17-A-I	200.6	120.0					37.8	34.6	0.92	0.49	0.74	1.50
	E20-A-I	202.3	102.2					35.5	32.6*	0.92	0.37	0.35*	0.94
	E10-B-I	200.0	200.0	35.8		0.34		58.9	54.0	0.92	1.43	1.21	0.85
	E10-B-II	201.1	201.1					53.3	53.9	1.01	0.95	1.20	1.27
	E13-B-I	202.9	156.0					47.9	49.7	1.04	1.02	1.11	1.08
	E13-B-II	200.7	155.4					56.3	50.1	0.89	0.96	1.11	1.16
	E17-B-I	200.8	120.2					57.2	45.1	0.79	1.31	0.99	0.75
	E17-B-II	199.9	120.9					59.4	45.4	0.76	1.29	0.99	0.77
	E20-B-I	202.9	102.1					44.2	40.9	0.93	0.82	0.86	1.05
	E20-B-II	200.3	101.9					46.3	41.3	0.89	0.89	0.88	0.98
	E10-C-I	200.2	200.2	46.4		0.17		52.3	51.1	0.98	0.64	0.75	1.17
	E10-C-II	200.1	200.1					52.9	51.1	0.97	0.63	0.75	1.19
	E13-C-I	203.2	156.7					51.1	48.6	0.95	0.74	0.70	0.95
	E13-C-II	201.3	155.0					52.5	48.7	0.93	0.71	0.71	1.00
	E17-C-I	201.0	120.1					49.7	46.4*	0.93	0.63	0.35*	0.55
	E17-C-II	200.0	121.1					51.1	46.4*	0.91	0.64	0.35*	0.55
	E20-C-I	202.1	102.3					48.1	46.4*	0.96	0.53	0.35*	0.67
	E20-C-II	200.5	102.2					46.8	46.4*	0.99	0.33	0.35*	1.08
	E10-D-I	200.3	200.3	40.2		0.34		57.8	57.8	1.00	0.80	1.13	1.42
	E10-D-II	200.1	200.1					64.0	57.8	0.90	1.02	1.13	1.11
	E13-D-I	203.5	156.4					59.1	53.5	0.91	0.98	1.04	1.06
	E13-D-II	201.7	154.7					59.6	53.6	0.90	0.89	1.04	1.17
	E17-D-I	200.6	120.3					59.0	48.9	0.83	1.18	0.93	0.79
	E17-D-II	200.0	121.1					54.3	49.1	0.90	0.74	0.94	1.27
	E20-D-I	202.3	102.1					50.8	44.6	0.88	0.98	0.82	0.84
	E20-D-II	200.6	102.0					52.0	44.9	0.86	0.66	0.83	1.27
	Average									**0.92**			**1.02**

Note: *= The concrete of that specimen was classified as insufficiently-confined, and therefore its stress-strain behaviour was taken to be that of unconfined concrete (i.e., Eqs. 1-3 with $f'_{cc} = f'_{co}$ and $\varepsilon_{cu} = 0.0035$)

Table 9 (part II). Performance of the proposed model against the test results of Ref. [12]

	Specimen	$2a$ (mm)	$2b$ (mm)	f'_{co} (MPa)	E_t (GPa)	t_f (mm)	$\varepsilon_{hu,circular}$ (%)	Experimental f'_{cc} (MPa)	Predicted f'_{cc} (MPa)	$f'_{cc,pre}/f'_{cc,exp}$	Experimental ε_{cu} (%)	Predicted ε_{cu} (%)	$\varepsilon_{cu,pre}/\varepsilon_{cu,exp}$
Ref. [12]	3C-1.0-I	250	250	72.4	210	0.50	1.54	104.0	97.1	0.93	1.69	1.58	0.94
	3C-1.0-I		250					105.7	97.1	0.92	1.91	1.58	0.83
	3C-1.3-I		192					90.5	88.2	0.97	1.67	1.45	0.87
	3C-1.3-II		192					87.0	88.2	1.01	1.59	1.45	0.91
	3C-1.7-I		147					80.4	77.0	0.96	1.29	1.25	0.97
	3C-1.7-II		147					77.6	77.0	0.99	1.07	1.25	1.17
	3C-2.0-I		125					76.8	72.4*	0.94	0.99	0.35*	0.35
	3C-2.0-II		125					76.5	72.4*	0.95	1.11	0.35*	0.32
	5G-1.0-I		250		72	1.77	1.27	106.5	100.7	0.95	1.50	1.43	0.95
	5G-1.0-II		250					110.4	100.7	0.91	1.55	1.43	0.92
	5G-1.3-I		192					93.9	92.2	0.98	1.18	1.32	1.12
	5G-1.3-II		192					93.9	92.2	0.98	1.30	1.32	1.02
	5G-1.7-I		147					82.5	81.3	0.99	1.02	1.14	1.12
	5G-1.7-II		147					83.7	81.3	0.97	0.95	1.14	1.20
	5G-2.0-I		125					78.3	73.6	0.94	0.90	1.00	1.11
	5G-2.0-II		125					76.2	73.6	0.97	0.86	1.00	1.16
	7G-1.0-I		250			2.48		136.3	120.2	0.88	2.26	1.77	0.78
	7G-1.0-II		250					136.8	120.2	0.88	2.07	1.77	0.86
	7G-1.3-I		192					111.1	108.5	0.98	1.59	1.61	1.01
	7G-1.3-II		192					113.4	108.5	0.96	1.51	1.61	1.07
	7G-1.7-I		147					95.3	93.4	0.98	1.21	1.39	1.15
	7G-1.7-II		147					97.1	93.4	0.96	1.08	1.39	1.28
	7G-2.0-I		125					87.3	82.6	0.95	1.06	1.20	1.13
	7G-2.0-II		125					88.8	82.6	0.93	1.03	1.20	1.17
	Average									**0.95**			**0.97**

Note: *= The concrete of that specimen was classified as insufficiently-confined, and therefore its stress-strain behaviour was taken to be that of unconfined concrete (i.e., Eqs. 1-3 with $f'_{cc} = f'_{co}$ and $\varepsilon_{cu} = 0.0035$).

Figures

(a) (b) (c)

Figure 1. Manufacturing of elliptical filament-wound tubes: (a) Elliptical steel moulds; (b) Filament-winding in progress; (c) FRP tubes ready for use

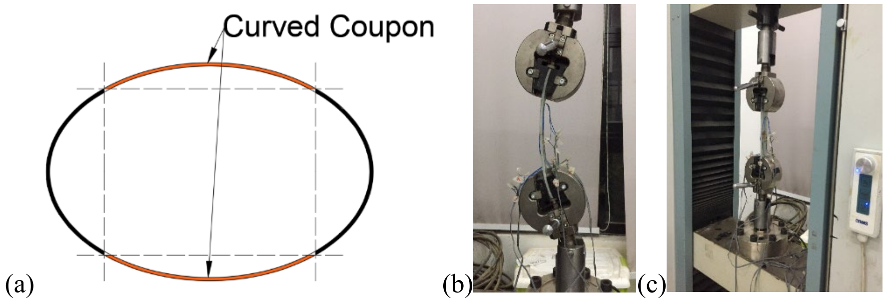

Figure 2. The curved coupon test: (a) Curved coupons from an FRP tube segment; (b) Curved coupon installed on an MTS machine; (c) Curved coupon test in progress

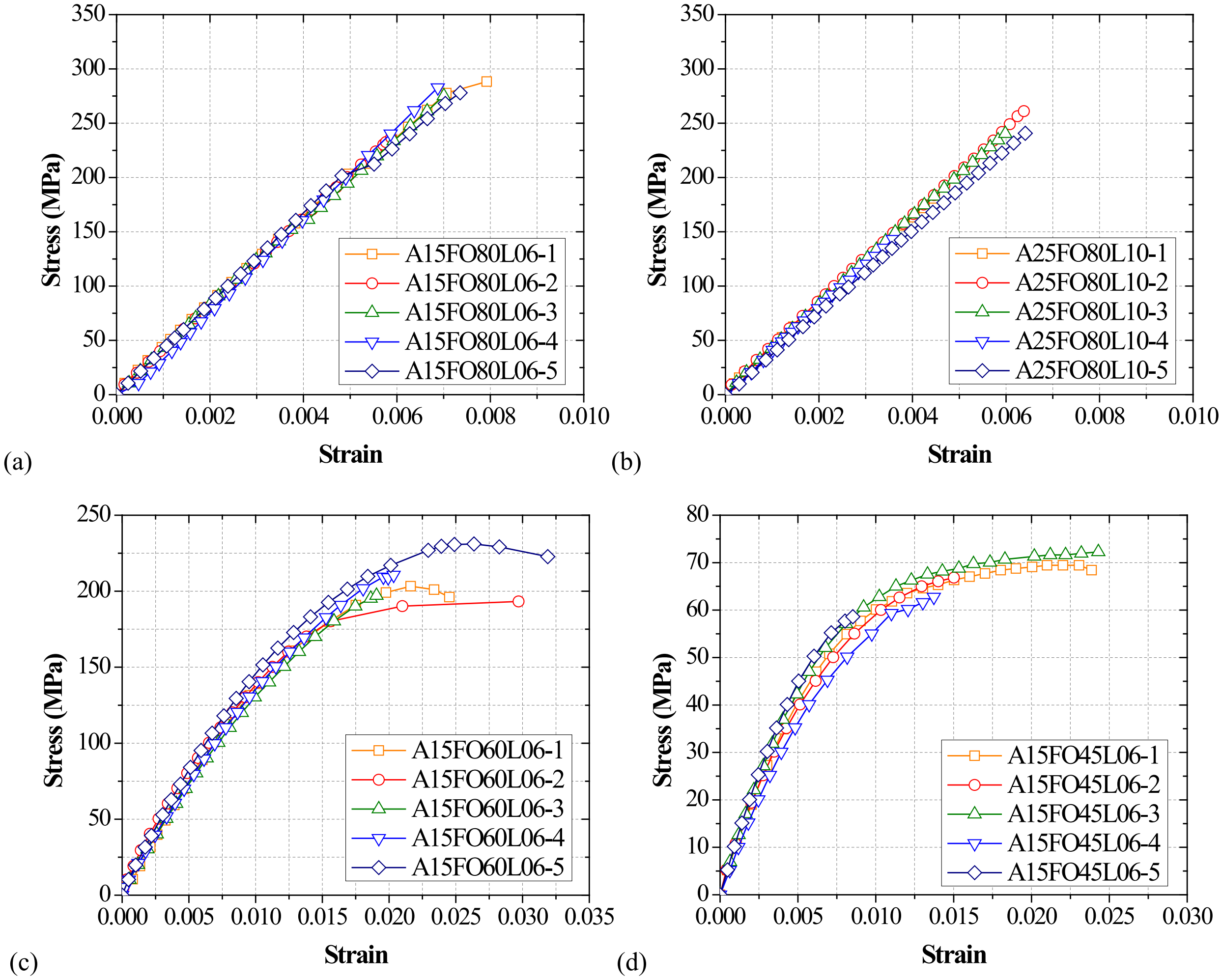

Figure 3. Stress-strain curves of curved coupons: (a) A15FO80L06; (b) A25FO80L10; (c) A15FO60L06; (d) A15FO45L06


(a) (b) (c)

Figure 4. Axial compression tests on FRP tube segments: (a) Test setup; (b) Failure mode; (c) Typical lateral expansion of a specimen with winding angles of ±60° or ±45°

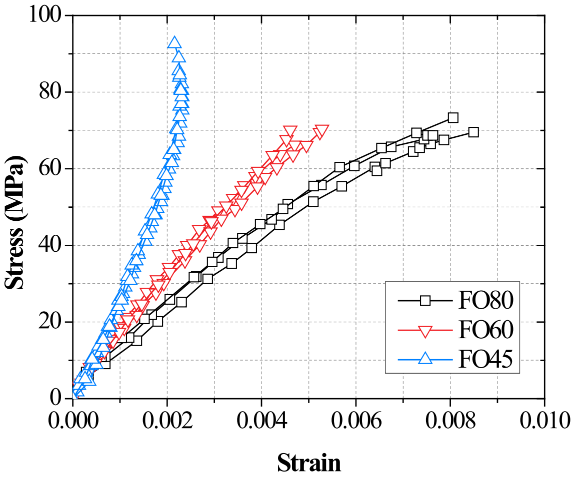

Figure 5. Stress-strain curves of FRP rings under axial compression

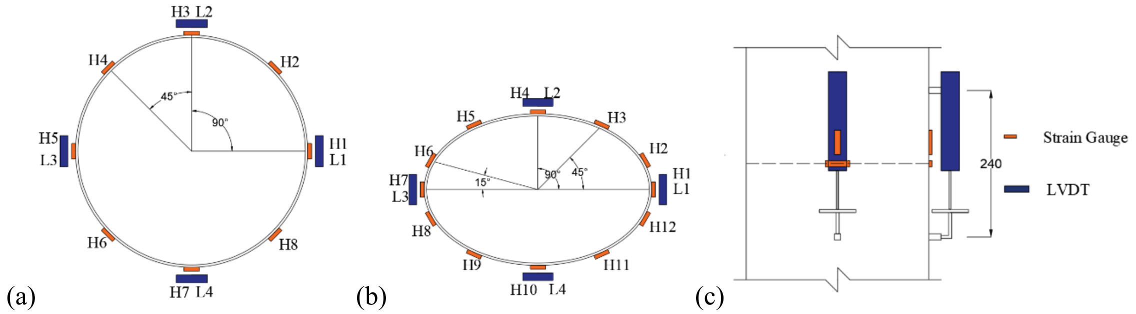

Figure 6. Layout of strain gauges and LVDTs: (a) Sectional configuration for a circular section; (b) Sectional configuration for an elliptical section; (c) Side configuration

Figure 7. Setup of compression tests on EFCCCs

E10B-L06-80 E15B-L06-80 E20B-L06-80 E25B-L06-80

(a) Specimens of batch B

E10D-L06-60 E15D-L06-60 E20D-L06-60 E25D-L06-60

(b) Specimens of batch D

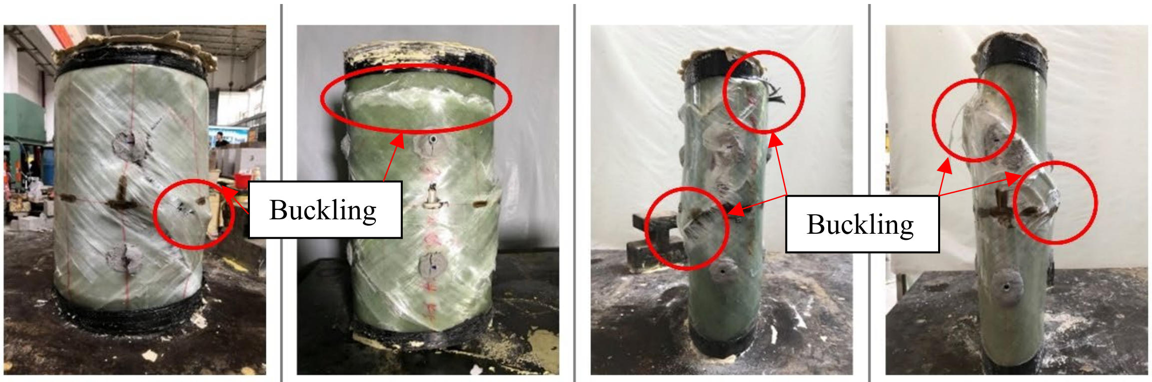

E10E-L06-45 E15E-L06-45 E20E-L06-45 E25E-L06-45

(c) Specimens of batch E

E25A-L06-80 E25B-L06-80

(d) Comparison between specimens E25A-L06-80 and E25B-L06-80

(e) Comparison between specimens E10A-L06-80 (right) and E10E-L06-45 (left)

E10B-L06-80 E15B-L06-80 E20B-L06-80 E25B-L06-80

(f) Specimens of batch B (without FRP tubes)

Figure 8. Failure modes of selected specimens

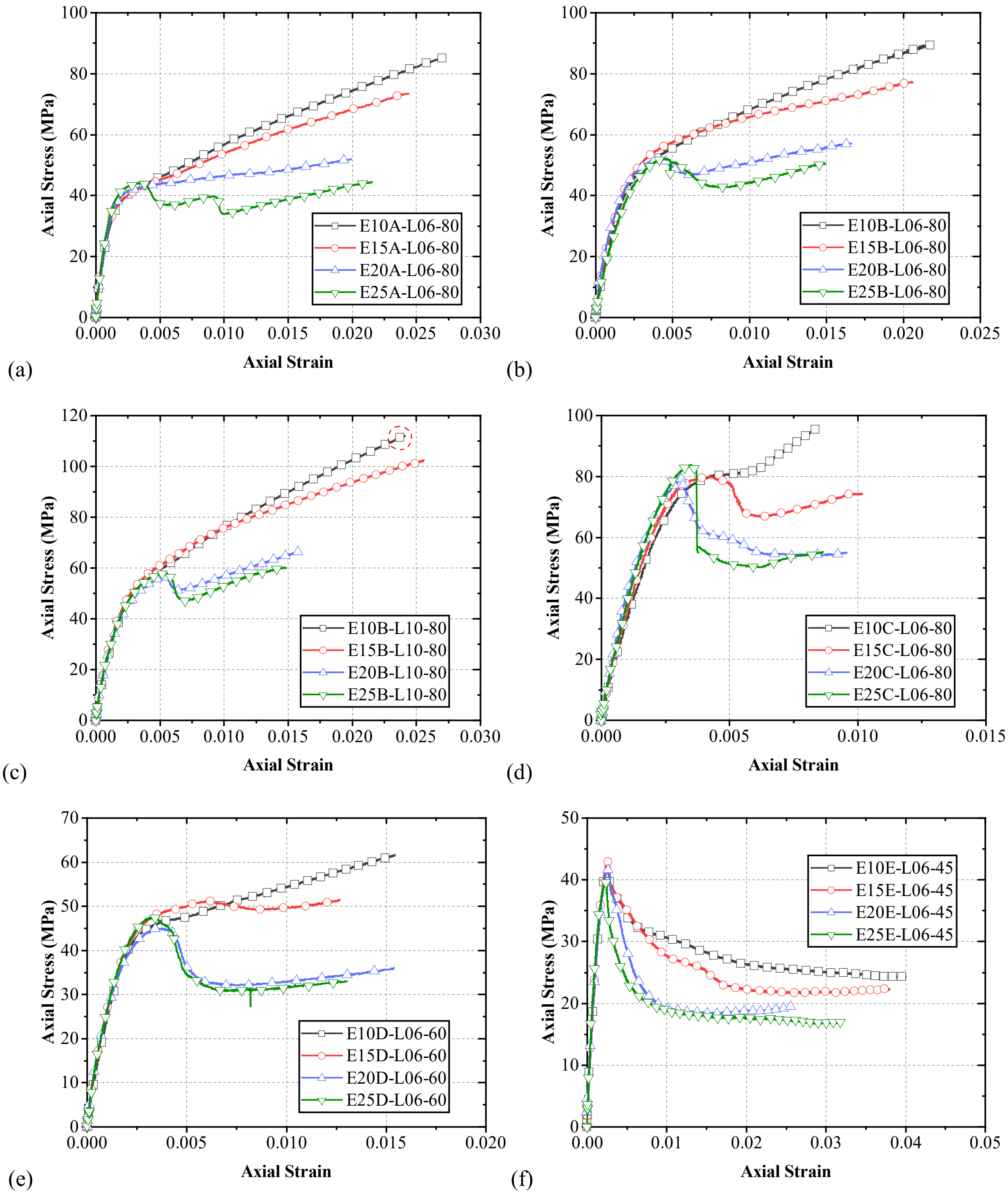

Figure 9. Axial stress-strain curves of EFCCC specimens: (a) batch A; (b) batch B with 6 fibre layers; (c) batch B with 10 fibre layers; (d) batch C; (e) batch D; (f) batch E

Notes:

1. Specimen E10B-L10-80 was not tested to failure due to the load capacity of the test machine, so the curve ends at the termination of the test as indicated by a circle;

2. The stress-strain curves in Figure 9f all end before failure as the LVDTs in these tests did not function properly at greater lateral expansions.

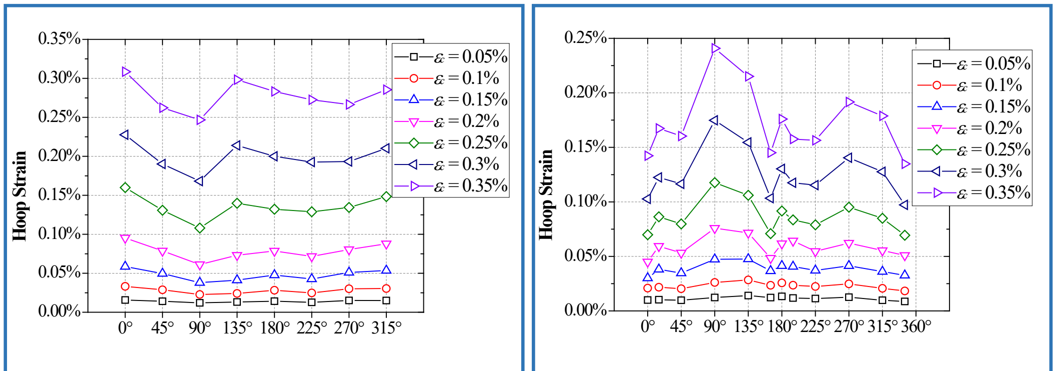

E10B-L06-80 (ε_c= 0.05%-0.35%)

E15B-L06-80 (ε_c= 0.05%-0.35%)

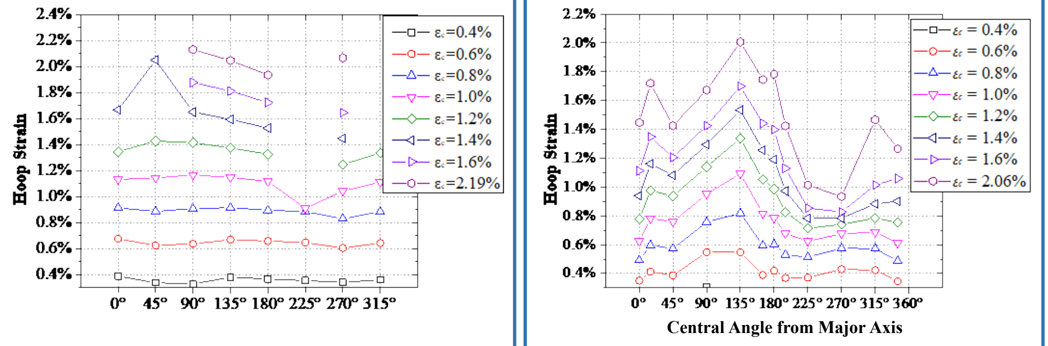

E10B-L06-80 (ε_c= 0.4%-2.19%)

E15B-L06-80 (ε_c= 0.4%-2.06%)

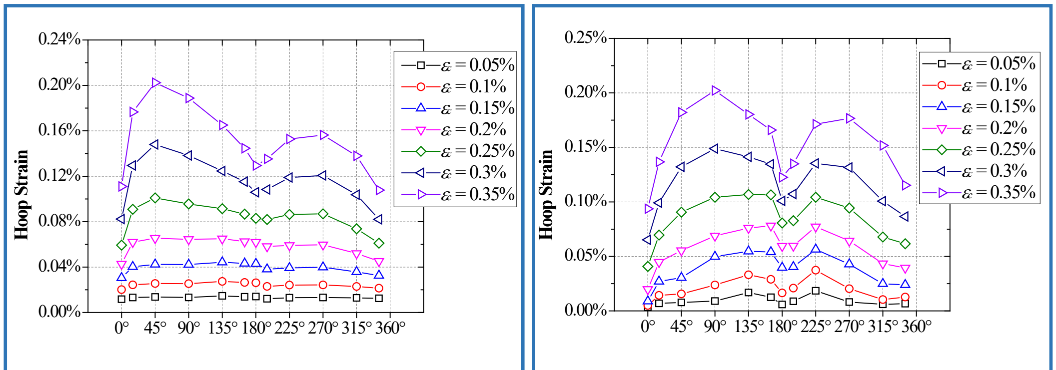

E20B-L06-80 (ε_c= 0.05%-0.35%)

E25B-L06-80 (ε_c= 0.05%-0.35%)

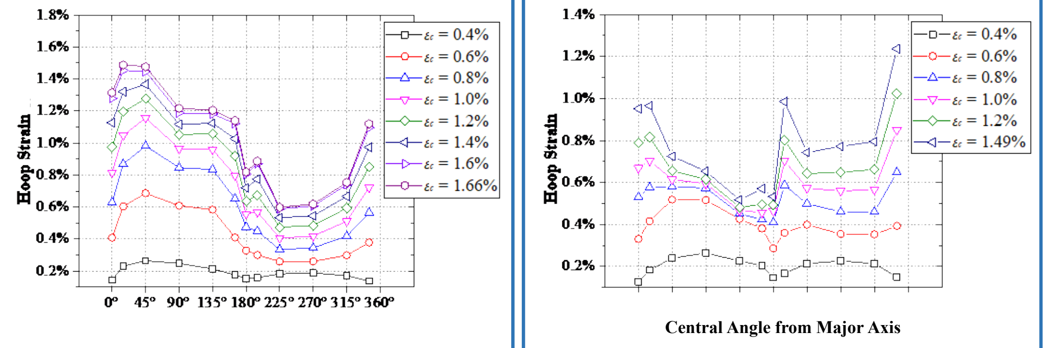

E20B-L06-80 (ε_c= 0.4%-1.66%)

E25B-L06-80 (ε_c= 0.4%-1.49%)

Figure 10. Hoop strain distributions in specimens of batch B

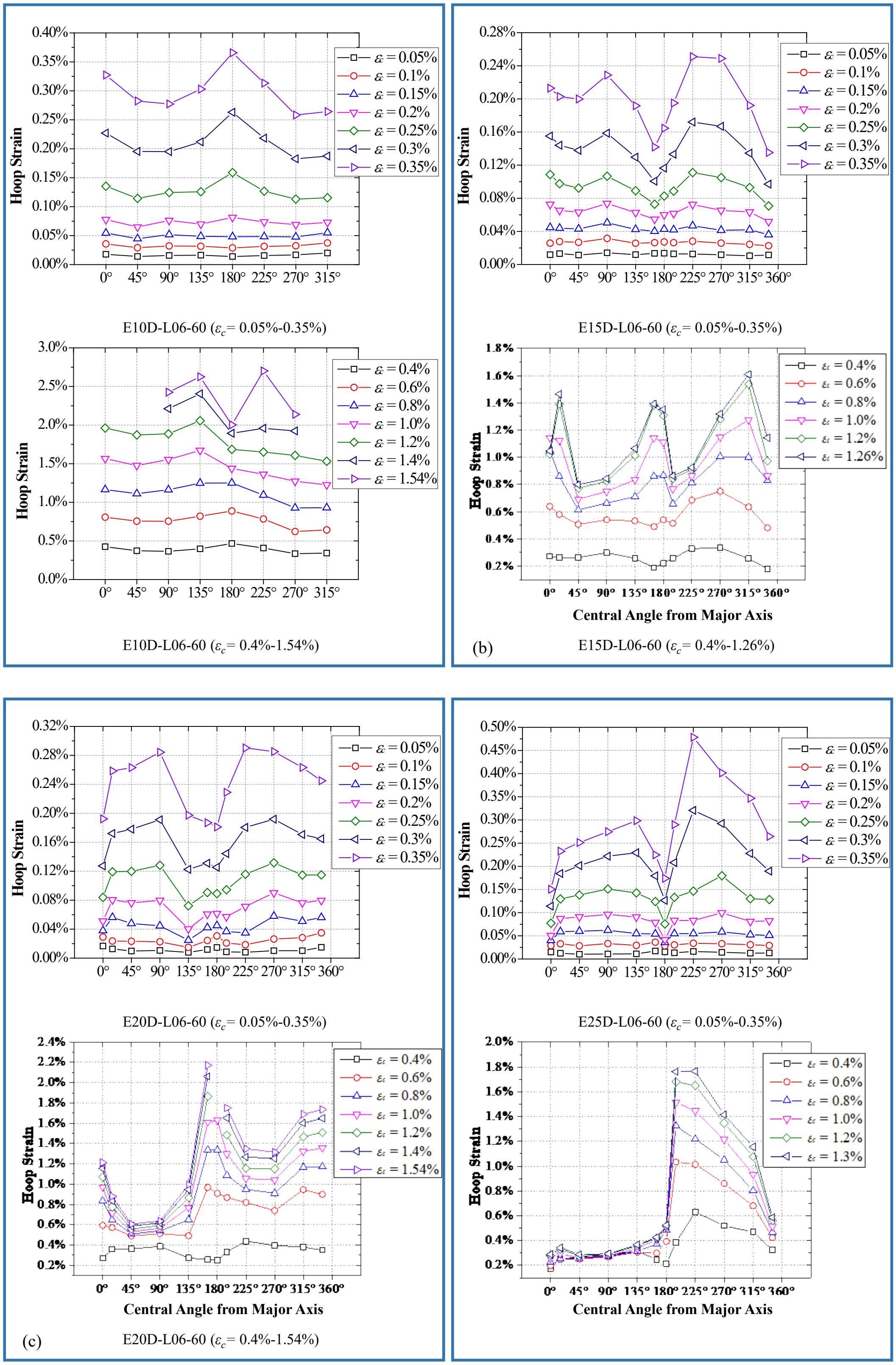

E10D-L06-60 (ε_c= 0.05%-0.35%)

E15D-L06-60 (ε_c= 0.05%-0.35%)

E10D-L06-60 (ε_c= 0.4%-1.54%)

(b) E15D-L06-60 (ε_c= 0.4%-1.26%)

E20D-L06-60 (ε_c= 0.05%-0.35%)

E25D-L06-60 (ε_c= 0.05%-0.35%)

(c) E20D-L06-60 (ε_c= 0.4%-1.54%)

Figure 11. Hoop strain distributions in specimens of batch D

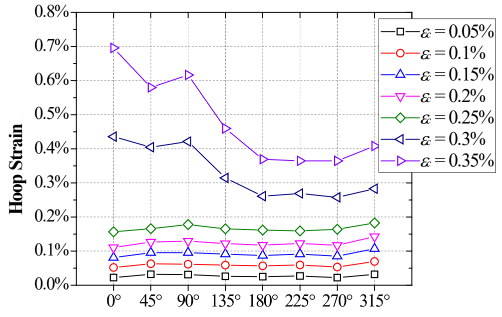

E10E-L06-45 (ε_c= 0.05%-0.35%)

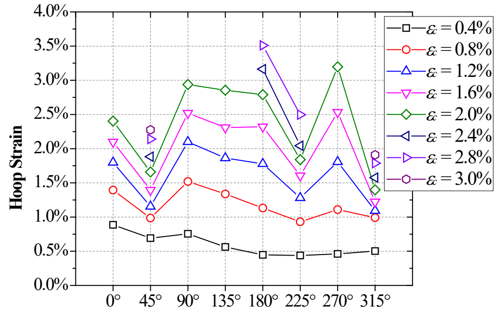

E10E-L06-45 (ε_c= 0.4%-3.0%)

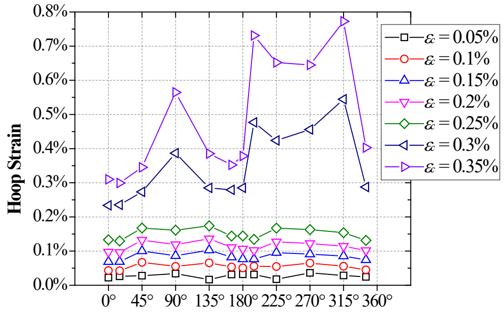

E15E-L06-45 (ε_c= 0.05%-0.35%)

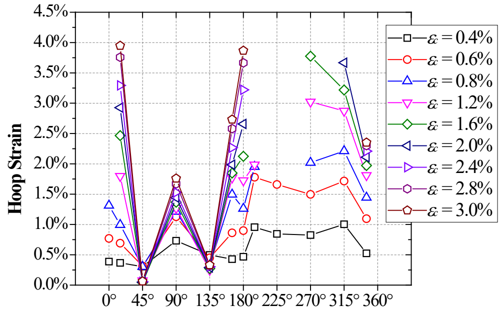

E15E-L06-45 (ε_c= 0.4%-3.0%)

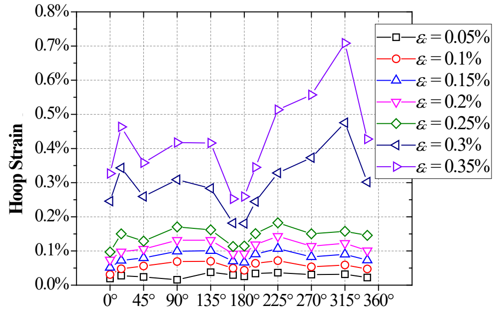

E20E-L06-45 (ε_c= 0.05%-0.35%)

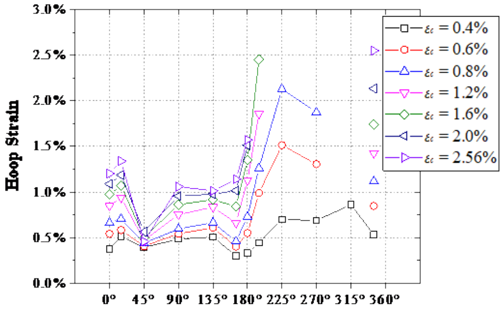

E20E-L06-45 (ε_c= 0.4%-2.56%)

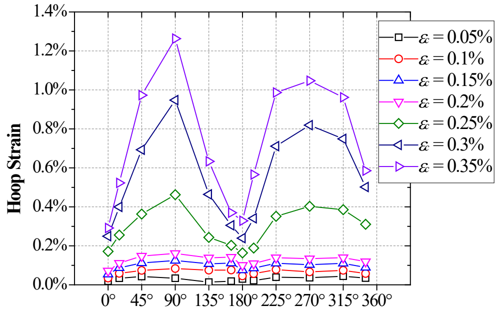

E25E-L06-45 (ε_c= 0.05%-0.35%)

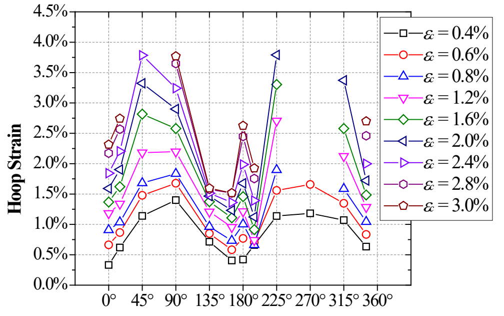

E25E-L06-45 (ε_c= 0.4%-3.0%)

Figure 12. Hoop strain distributions in specimens of batch E

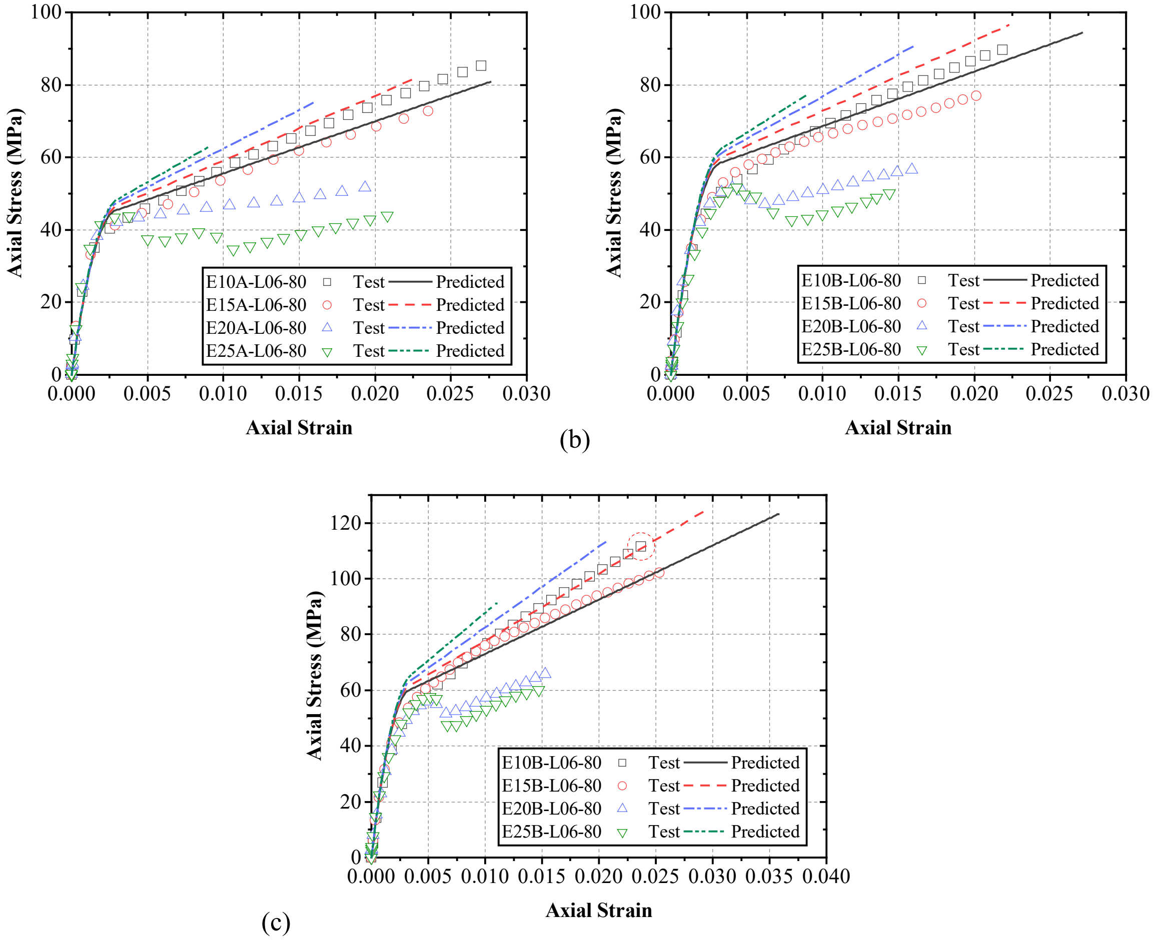

(a) (b)

(c)

Figure 13. Test stress-strain curves versus predictions of Teng et al.'s model [11]: (a) batch A specimens; (b) batch B specimens with 6 fibre layers; (c) batch B specimens with 10 fibre layers

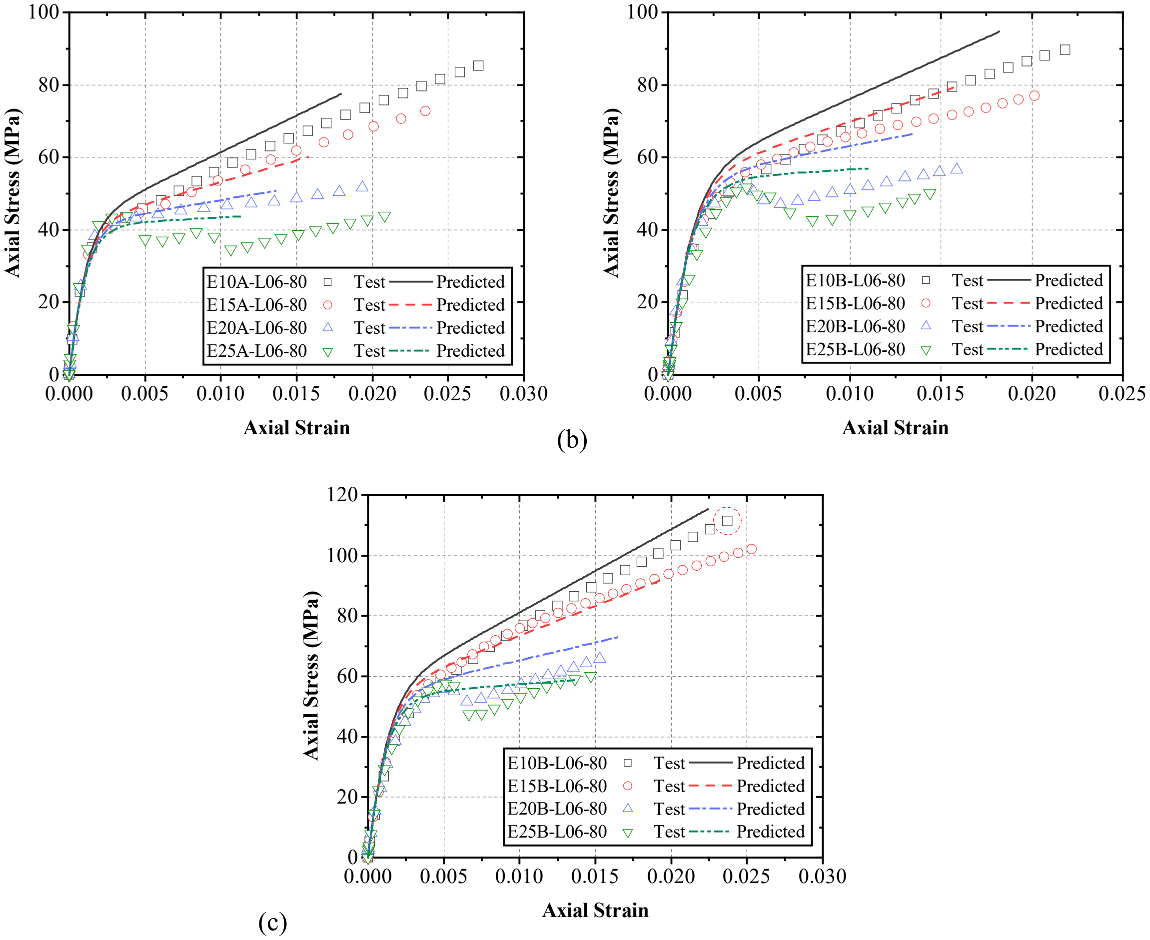

(a) (b)

(c)

Figure 14. Test stress-strain curves versus predictions of Cao et al.'s model [14]: (a) batch A specimens; (b) batch B specimens with 6 fibre layers; (c) batch B specimens with 10 fibre layers

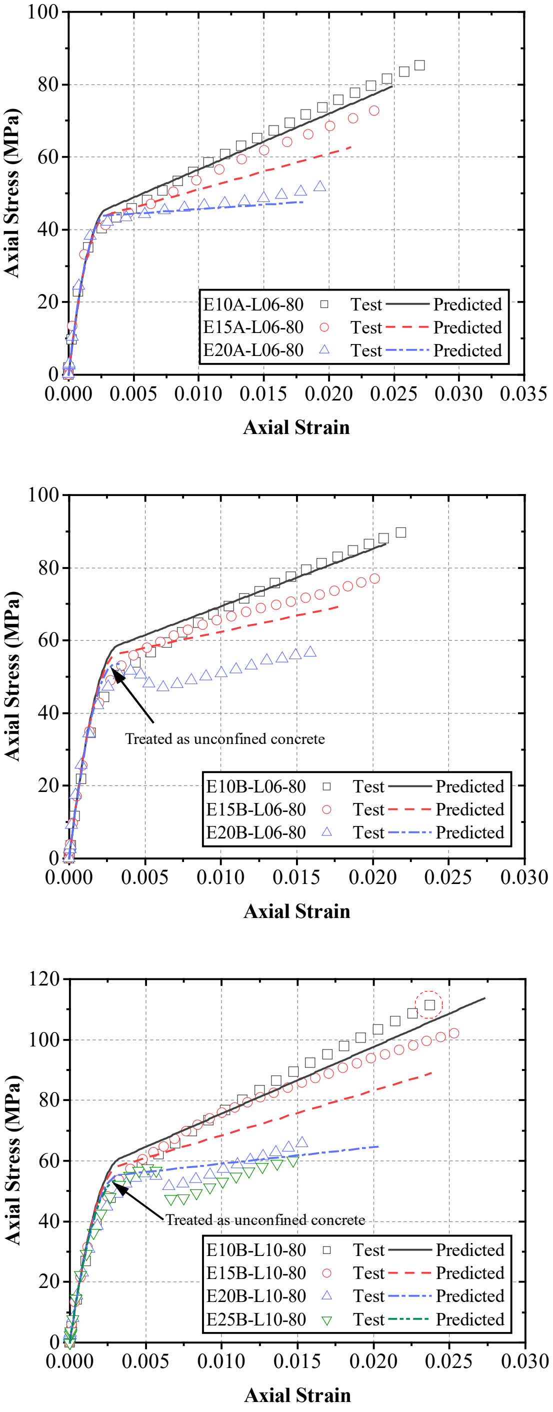

(a)

(b)

(c)

Figure 15. Test stress-strain curves versus predictions of GB50608's model [17]: (a) batch A specimens; (b) batch B specimens with 6 fibre layers; (c) batch B specimens with 10 fibre layers

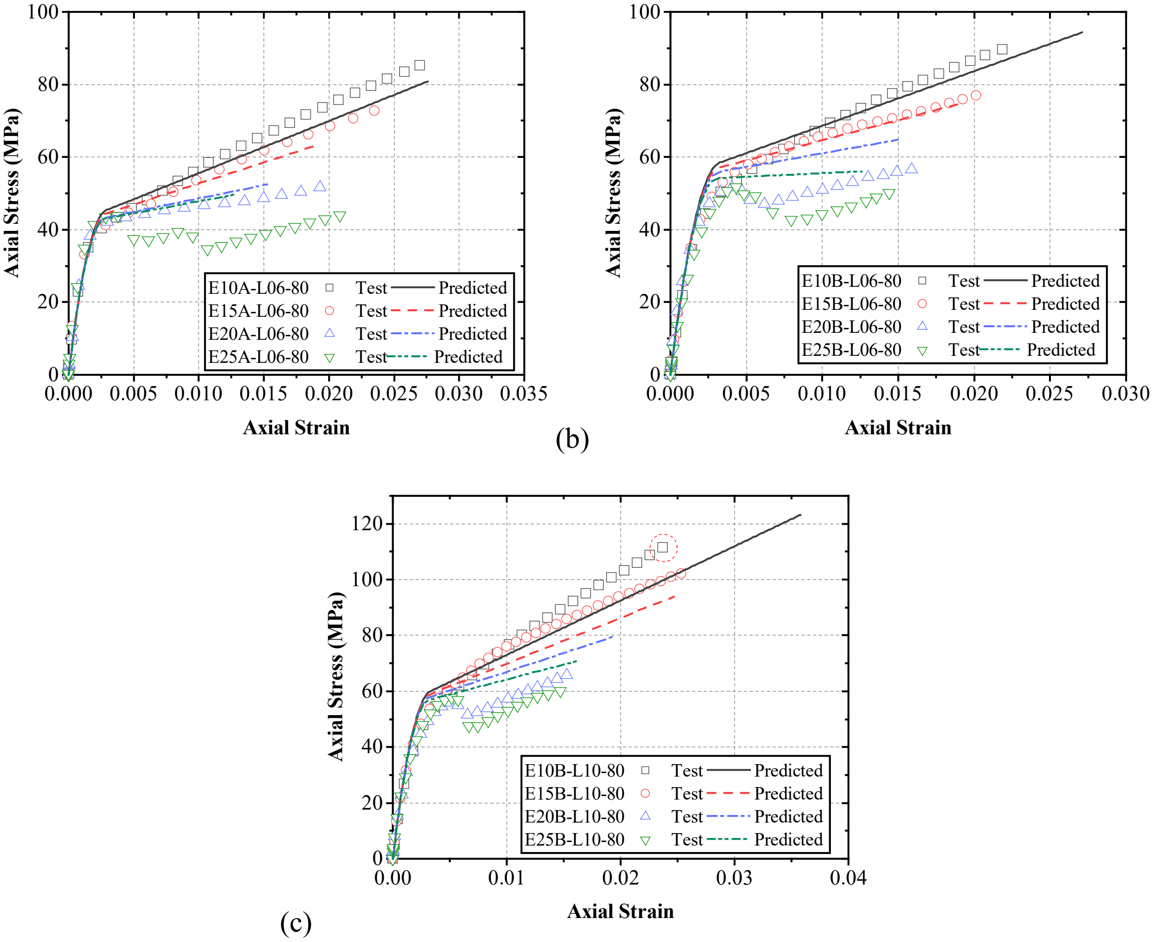

(a) (b)

(c)

Figure 16. Test stress-strain curves versus predictions of Chen et al.'s model [12]: (a) batch A specimens; (b) batch B specimens with 6 fibre layers; (c) batch B specimens with 10 fibre layers

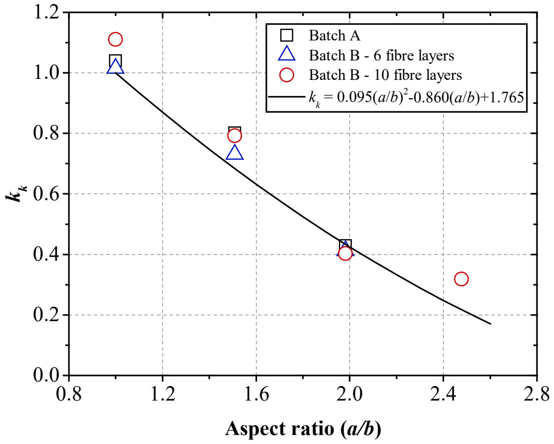

Figure 17. Development of equation for k_k

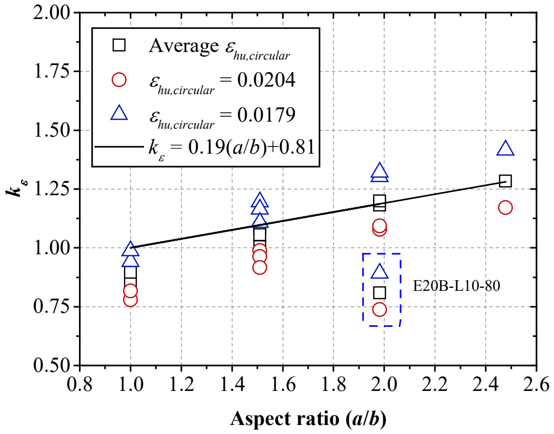

Figure 18. Development of equation for k_ε

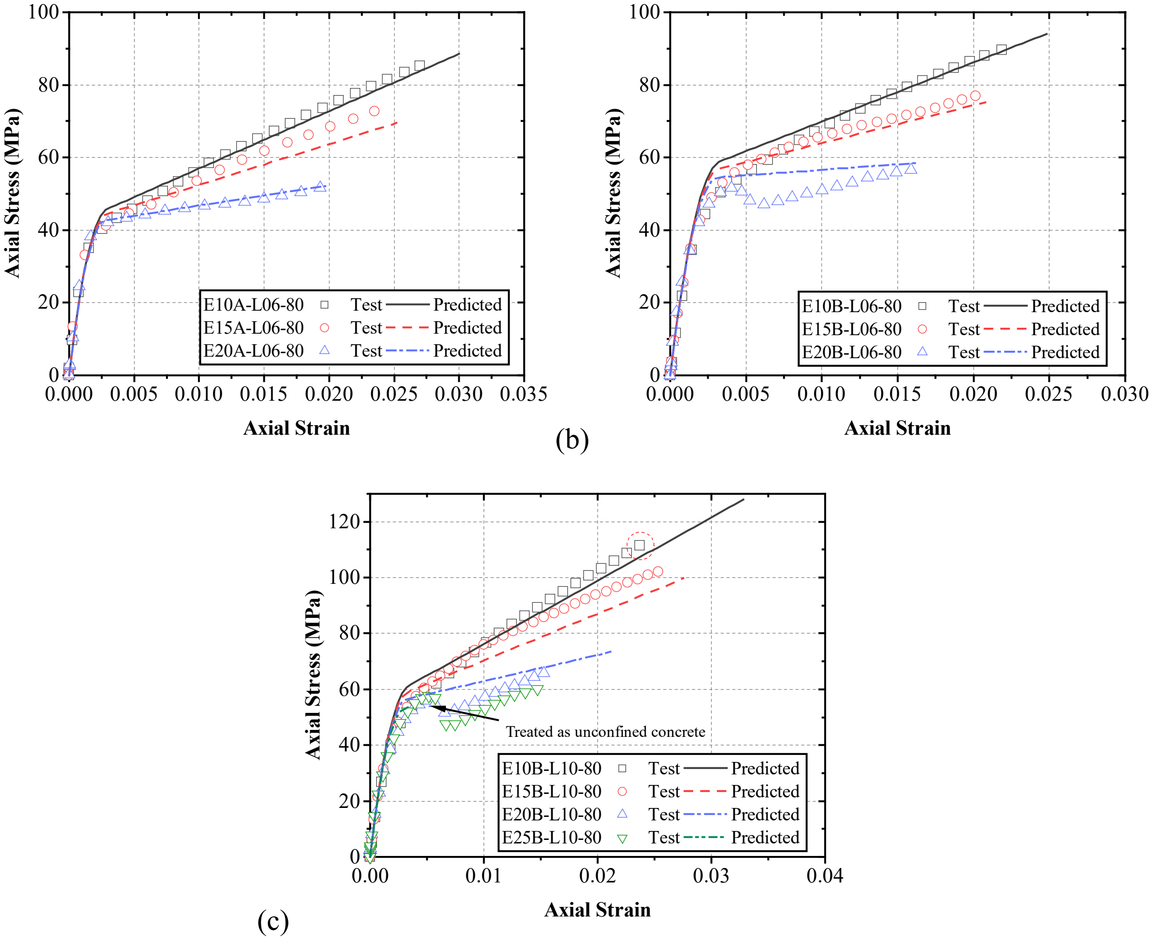

(a)

(b)

(c)

Figure 19. Test stress-strain curves versus predictions of the proposed model: (a) batch A specimens; (b) batch B specimens with 6 fibre layers; (c) batch B specimens with 10 fibre layers

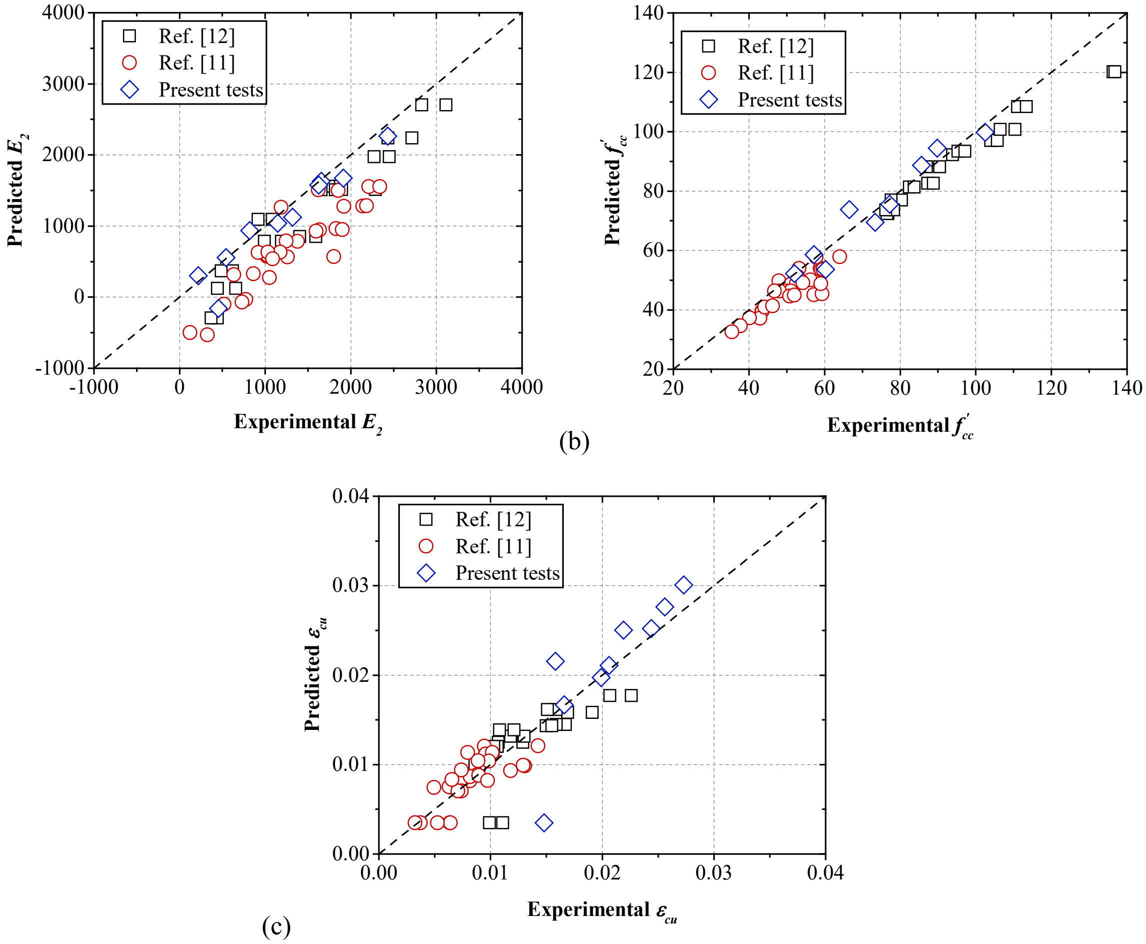

(a) (b)

(c)

Figure 20. Comparisons between test results and predictions of the proposed model: (a) second-stage stiffness, E_2; (b) axial strength of confined concrete, f'_{cc}; (c) ultimate axial strain of confined concrete, ε_{cu}.

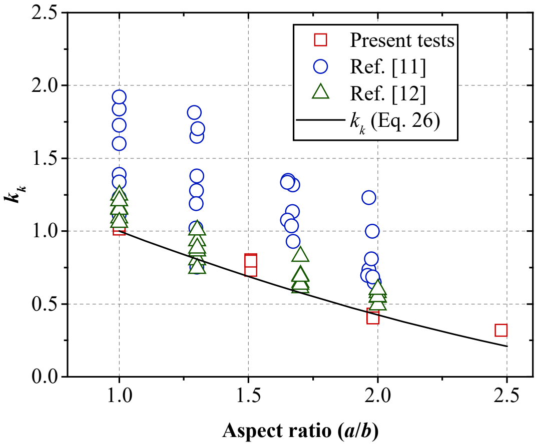

Figure 21. Comparison between the experimental k_k and the prediction of Eq. 26

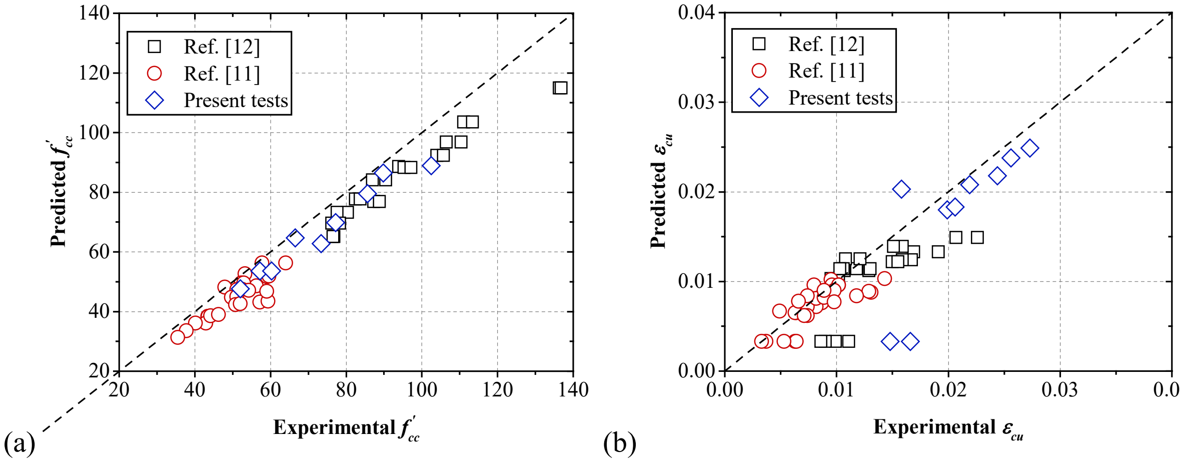

Figure 22. Comparisons between test results and predictions of G50608's model [17]: (a) axial strength of confined concrete, f'_{cc}; (b) ultimate axial strain of confined concrete, ε_{cu}.